Quantifying uncertainty in inverse scattering problems set in layered environments

Carolina Abugattas, Ana Carpio, Gerardo Oleaga,
Universidad Complutense de Madrid, Spain

Elena Cebrián, Universidad de Burgos, Spain

April 9, 2025

Abstract. The attempt to solve inverse scattering problems often leads to optimization and sampling problems that require handling moderate to large amounts of partial differential equations acting as constraints. We focus here on determining inclusions in a layered medium from the measurement of wave fields on the surface, while quantifying uncertainty and addressing the effect of wave solver quality. Inclusions are characterized by a few parameters describing their material properties and shapes. We devise algorithms to estimate the most likely configurations by optimizing cost functionals with Bayesian regularizations and wave constraints. In particular, we design an automatic Levenberg-Marquardt-Fletcher type scheme based on the use of algorithmic differentiation and adaptive finite element meshes for time dependent wave equation constraints with changing inclusions. In synthetic tests with a single frequency, this scheme converges in few iterations for increasing noise levels. To attain a global view of other possible high probability configurations and asymmetry effects we resort to parallelizable affine invariant Markov Chain Monte Carlo methods, at the cost of solving a few million wave problems. This forces the use of prefixed meshes. While the optimal configurations remain similar, we encounter additional high probability inclusions influenced by the prior information, the noise level and the layered structure, effect that can be reduced by considering more frequencies.

Keywords. Inverse scattering problems, Partial differential equations, Constrained optimization, Wave equations, Adaptive methods, Bayesian inverse problems, Uncertainty quantification.

1 Introduction

Geophysical imaging is a noninvasive imaging technique that investigates the subsurface. It uses elastic waves created by man-made explosions and vibrations to image the subsurface of Earth [56]. Elastic waves split in two components [40, 53]. Compression waves (P-waves) are longitudinal in nature and penetrate through subsurface layers, causing the ground to compress and stretch along the axis of propagation of the

wave in a similar way to sound waves. Due to these properties, longitudinal P-waves constitute a useful tool for underground imaging at considerable depth.

Figure 1 represents the structure of a standard imaging set-up. Explosions or strong impacts at certain locations produce elastic waves that propagate under the surface. These waves interact with subsurface structures and are reflected at different depths [25, 53, 56, 57]. Then, a grid of recording devices measures the reflected waves. Different procedures have been developed to image subsurface layer properties, such as classical seismic reflection and full waveform inversion [56, 58]. Assuming that the basic layered structure has been already characterized by other techniques [53, 60], our goal here is to refine the description of localized inclusions of different materials with quantified uncertainty, which leads to solving an inverse scattering problem.

Inverse scattering problems share a similar mathematical structure: a number of sources launch waves that interact with a medium containing scatterers and the resulting waves are recorded at a set of detectors. Knowing the recorded signals we aim to identify the scatterers. Methods are adapted to the nature of the waves and the way the inclusion properties are represented mathematically, see [2, 5, 8, 9, 12, 18, 24, 33, 35, 39, 41] and references therein, for example. Waves can be time-harmonic, and thus governed by stationary elliptic problems, or time dependent (thermal, electromagnetic, acoustic...). Physical properties can be represented as infinite dimensional coefficient functions, high dimensional sets of values at grid points, level set functions or localized star-shaped inclusions, for instance. Inverse scattering problems are severely ill-posed and are often regularized by means of variational formulations [13, 24]. A variety of deterministic approaches are based on minimizing cost functionals which compare the recorded data with the synthetic data that would be obtained for arbitrary scatterers, as predicted by a selected forward model for the propagation of the emitted waves. Optimization strategies employed often implement total variation regularizations, Tikhonov regularizations or iteratively regularized Gauss Newton approaches [9, 16, 23, 30, 34], and may rely on distances other than the Euclidean, i.e. Wasserstein distances [59].

In practice, recorded data are affected by noise. Typically, deterministic strategies produce the best solution for a given dataset, that is, a given realization of noise. However, we lack information on how the proposed solution can change as we vary the noise realizations. Under some conditions, deterministic iteratively regularized Gauss Newton methods can provide approximate solutions that are acceptable within a noise level [34]. Instead, Bayesian formulations of the inverse problem aim to provide the most likely solutions while quantifying uncertainty about them for a given noise magnitude. Statistical inverse problems also require the choice of a mathematical representation of the unknown fields, see [6, 11, 20, 47, 60] for high dimensional sets of values at grid points, level set functions or localized star-shaped inclusions, for instance. In a Bayesian context, the problem can be addressed by Markov Chain Monte Carlo (MCMC) techniques or Laplace approximations [27, 43]. In contrast with infinite dimensional formulations [6, 7, 21, 54], we will focus here on situations in which the inclusions are characterized by a finite and fixed number of random variables. Our goal is to devise automatic procedures and assess specific issues related to the practical choice of time dependent wave equation solvers. Furthermore, this choice allows us to study at a reasonable computational cost the appearance of several
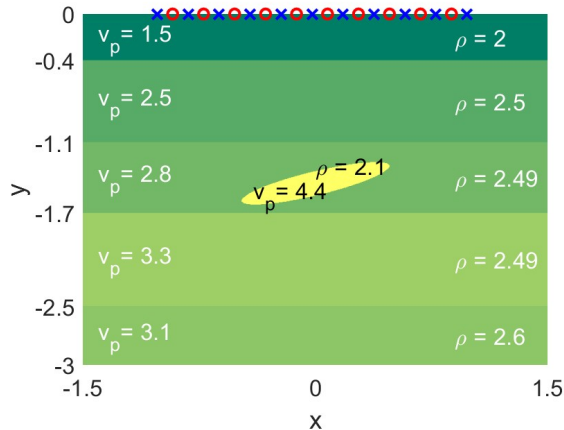
2

Figure 1: Schematic representation of an imaging set-up. The emitters (red) generate waves which interact with the medium. The reflected waves are recorded at the receivers (blue). The velocities are in units of 10^3 m/s and the densities in units of kg/m^3. Units for x and y are km. Parameter values are typical of sandstone, shale, limestone, and salt for the inclusion.

high probability configurations and how we can modify the imaging set up to eliminate spurious ones, reducing uncertainty in this way.

Success of both deterministic and statistical approaches to the numerical solution of inverse scattering problems relies on being able to solve moderate to large amounts of auxiliary boundary value problems modeling wave propagation. The configuration under here study (see Figure 1) shows abrupt changes at interfaces between materials of a different nature, which are described as discontinuities in the fields representing physical properties. In time-harmonic problems, efficient boundary element solvers are available [9, 32, 35], which are usually applied to inclusions in homogeneous backgrounds. For time dependent problems, boundary element methods are less developed [31]. Moreover, in our layered geometry, interfaces arise not only around the sought inclusions, but in the surrounding environment too. When we employ finite element (FEM) solvers for wave equations of the form $\rho(\mathbf{x})u_{tt} - \mathrm{div}(\chi(\mathbf{x})\nabla u) = h$, with piecewise fields ρ and χ representing the density and elastic constants of different materials, the question arises of whether to keep a fixed mesh (which increases the error at discontinuities) or adapt the mesh to the varying interfaces (which increases the computational cost) and whether this choice has a relevant effect on the results in our context, since it may affect the speed of propagation when crossing layers [1].

---

[1]Some work in the literature, such as [21], use wave constraints of the form $m(\mathbf{x})u_{tt} - \Delta u = h$ thinking of $m^{-1/2} = v_\mathrm{p}$ as the wave velocity, instead of $\rho(\mathbf{x})u_{tt} - \mathrm{div}(\chi(\mathbf{x})\nabla u) = h$. When the density ρ and elastic parameters χ are constant everywhere, we can indeed write such an equation for the waves, with constant m and $v_\mathrm{p} = \sqrt{\chi/\rho}$, see Appendix. If χ varies spatially, we cannot. Furthermore, in medical applications, for instance, we can set $\rho \sim 1$ and work with one field instead of two [11]. In geophysical applications, we must keep two fields, either $\rho(\mathbf{x})$ and $\chi(\mathbf{x})$ or $\rho(\mathbf{x})$ and

In this paper, we develop techniques to estimate the most likely inclusions given noisy data, characterized as minima of cost functionals constrained by time dependent wave equations with a Bayesian regularization. Regularizing terms are expected to convexify the cost functionals, still, local minima may persist depending on the quality of the prior information and the imaging set-up design. We consider three approaches, which provide complementary information. First, we propose an automatic adaptive optimization scheme that combines Levenberg-Marquardt [26, 44] type iterations with the use of adaptive meshes [48, 49] for finite element discretization of the wave constraint and automatic differentiation [52] to quantify variations in the proposed inclusions at each stage. The resulting adaptive scheme is fully automatic: the user must only provide the data, the noise level, and the prior information. This algorithm usually converges to the main minimum in a few iterations in the tests we have performed. Second, we introduce an alternative scheme based on FEM discretizations of the wave constraint on fine enough prefixed stratified or uniform meshes. This algorithm employs finite difference approximations of the observation operator defined by the wave problems as we modify the inclusions to seek descent directions. Varying the step, we reach the global minimum but could also identify some additional local minima if present. Finally, we resort to affine invariant MCMC samplers [28] to characterize all minima in detail. Adaptive meshes are currently not affordable within MCMC schemes, therefore we employ again fixed uniform or stratified meshes. The optimal configurations encountered by the three methods are similar in the synthetic tests we have carried out. We obtain basic uncertainty estimates on parameter ranges resorting to the so-called Laplace approximation, by linearizing about the optimal inclusions. Unlike what happens in similar imaging set-ups for medical applications in homegeneous backgrounds [11] when employing one frequency, here MCMC techniques identify several high probability configurations, regardless of the use of uniform (blind to the layered structure) or stratified (adapted to the known layered structure but not to the scatterer) meshes. Provided the meshes are fine enough, their effect on the hight probability configurations remains small. The highest probability estimate resembles the true inclusion. Secondary configurations seem to reflect the interaction with the layered structure, a memory of the prior information, the difficulty to resolve depth in this type of imaging set-ups with one sided information and the noise to signal ratio. The appearance of 'phantom' inclusions in uncertainty studies has been related to aberrations caused by lack of information from enough incidence directions [10] in optical applications. Here, we notice that the use of data recorded for different frequencies helps to convexify the cost and reduces the uncertainty caused by secondary modes.

The paper is organized as follows. We describe the imaging set-up and state the inverse problem in Section 2. Section 3 formulates finite dimensional approximations obtained discretizing the forward problem for wave propagation and the observation operator. In Section 4, we develop optimization approaches to estimate the most likely inclusions given noisy data. After testing the performance of the algorithms

---

$\rho(\mathbf{x})v_{\mathrm{p}}(\mathbf{x})^2$ [7]. Reference [21] analyzes the performance of different distances in the costs/likelihoods in uncertainty studies in a two dimensional geometry similar to ours, but working in an infinito-dimensional framework with a more or less homogeneous background. However, their choice of wave constraint $mu_{tt} - \Delta u = h$ removes one of the two fields characterizing the media and the inclusions.

with synthetic data, in Section 5 we quantify uncertainty in the inclusion parameter predictions by Laplace approximations and by MCMC sample analysis. We choose a practical test of current interest in geological studies: the characterization of a salt inclusion, which usually hide reservoirs of raw materials [19]. Lastly, Section 6 summarizes our conclusions. Appendix A collects details on the nondimensionalization of the model and the parameters selected. Appendix B formulates a well posedness theory for the truncated wave problem with artificial boundary conditions we use as constraint. Finally, Appendix C describes the numerical schemes we implement to approximate its solutions and discusses their convergence properties.

2 Object based full-waveform inversion

Consider an imaging set-up as depicted in Figure 1. A grid of sources, $\mathbf{x}_k$, $k = 0, \ldots, K$, emits waves that propagate under the ground, interact with subsurface structures, are reflected and recorded again on the surface, at an interspaced grid of receivers $\mathbf{r}_j$, $j = 0, \ldots, J$. Here, we assume that we have information on the layered structure. The goal is to characterize localized inclusions of different materials given the data $\mathbf{d}$ recorded at the receivers at a sequence of times t_m, $m = 1, \ldots, M$. These scatterers are often described by a finite collection of parameters $\boldsymbol{\nu}$ representing their material parameters and geometry [1, 9, 30, 32, 47]. To identify $\boldsymbol{\nu}$ from measurements $\mathbf{d}$ we first need to relate both by means of a mathematical model of wave propagation and a suitable observation operator.

2.1 Observation operator

In a simple model of longitudinal wave propagation, the waves emitted by the sources are governed by a scalar wave equation:

$$
\begin{aligned}
\rho\, u_{tt} &= \mathrm{div}[(\lambda + 2\mu)\nabla u] + \rho(\mathbf{x})h & \mathbf{x} &\in \mathcal{R},\, t > 0, \\
\nabla u \cdot \mathbf{n} &= 0, & \mathbf{x} &\in \Sigma,\, t > 0, \\
u(0, \mathbf{x}) &= 0,\ u_t(0, \mathbf{x}) = 0, & \mathbf{x} &\in R.
\end{aligned} \tag{1}
$$

Here, the subsurface is represented by a half-space $\mathcal{R}$ and $u(\mathbf{x}, t)$ denotes downward displacements in the direction y, with $\mathbf{x} = (x, y)$. We model the emitters as source terms of the form $f(t)g(\mathbf{x} - \mathbf{x}_k)$, $k = 1, \ldots, K$. The function $f(t)$ is a Ricker wavelet $f(t) = f_0(1 - 2\pi^2 f_M^2 t^2)e^{-\pi^2 f_M^2 t^2}$ with peak frequency f_M. The function g has a narrow support and zero normal derivative at $y = 0$. For instance, we may set $h(t, \mathbf{x}) = f(t)G(\mathbf{x}) = \frac{f_0 f(t)}{(\pi \kappa)^{n/2}} \sum_{k=1}^{K} \exp(-\frac{|\mathbf{x} - \mathbf{x}_k|^2}{\kappa})$, $n = 2$.

In a layered geometry, the density $\rho(\mathbf{x})$ and the elastic constants $\lambda(\mathbf{x})$ and $\mu(\mathbf{x})$ are piecewise constant in $\mathcal{R}$. When additional inclusions $\Omega_{\boldsymbol{\nu}} = \cup_{\ell=1}^{L}\Omega^{\ell}$ of different materials are present we set

$$
\rho(\mathbf{x}) = \begin{cases} \rho, & \mathbf{x} \in \mathcal{R} \setminus \overline{\Omega}_{\boldsymbol{\nu}}, \\ \rho_{\mathrm{i}}^{\ell}, & \mathbf{x} \in \Omega^{\ell},\ \ell = 1, \ldots, L, \end{cases} \tag{2}
$$

$$
\chi(\mathbf{x}) = \begin{cases} \lambda + 2\mu = \rho v_{\mathrm{p}}^2, & \mathbf{x} \in \mathcal{R} \setminus \overline{\Omega}_{\boldsymbol{\nu}}, \\ \lambda_{\mathrm{i}}^{\ell} + 2\mu_{\mathrm{i}}^{\ell} = \rho_{\mathrm{i}}^{\ell}(v_{\mathrm{p,i}}^2)^{\ell}, & \mathbf{x} \in \Omega^{\ell},\ \ell = 1, \ldots, L, \end{cases} \tag{3}
$$

where v_p is the wave speed in each of the subdomains.

Measurements can be related to wave models in different ways depending on the set-up. Here we assume that the measured data correspond to values taken by the solution of (1) at the receivers. Given inclusions characterized by parameters $\boldsymbol{\nu}_\mathrm{true}$, the corresponding data $\mathbf{d}_\mathrm{true}$ are related to $\boldsymbol{\nu}_\mathrm{true}$ through the observation operator

$$
\begin{aligned}
\mathbf{o}: \quad &\mathbb{R}^P \longrightarrow \mathbb{R}^D \\
&\boldsymbol{\nu} \longrightarrow (u_{\boldsymbol{\nu}}(\mathbf{r}_j, t_m))_{j=1,\ldots,J, m=1,\ldots,M},
\end{aligned}
\tag{4}
$$

where $u_{\boldsymbol{\nu}}$ stands for the solution of (1), P is the number of parameters and the number of data is $D = MJ$. We expect the data $\mathbf{d}_\mathrm{true}$ recorded for inclusions parametrized by $\boldsymbol{\nu}_\mathrm{true}$ to satisfy $\mathbf{o}(\boldsymbol{\nu}_\mathrm{true}) = \mathbf{d}_\mathrm{true}$. In practice, the recorded data are corrupted by noise:

$$
\mathbf{d} = \mathbf{o}(\boldsymbol{\nu}_\mathrm{true}) + \boldsymbol{\varepsilon}, \quad \boldsymbol{\eta} \sim \mathcal{N}(0, \boldsymbol{\Gamma}_\mathrm{n}).
\tag{5}
$$

We assume that $\boldsymbol{\varepsilon}$ is distributed as a multivariate Gaussian.

2.2 Deterministic inverse problem

Given data $\mathbf{d}$, the inverse problem consists in finding the parameters $\boldsymbol{\nu}$ for which the observed data $\mathbf{d} = \mathbf{o}(\boldsymbol{\nu})$. This is a severely ill posed problem [13] which is often regularized by means of constrained optimization reformulations aiming to optimize a cost [4]

$$
J(\boldsymbol{\nu}) = J_\mathrm{d}(\boldsymbol{\nu}) + \mathcal{R}(\boldsymbol{\nu}), \quad J_\mathrm{d}(\boldsymbol{\nu}) = \frac{1}{2} \sum_{j=1}^{J} \sum_{m=1}^{M} |u_{\boldsymbol{\nu}}(r_j, 0, t_m) - d_j^m|^2,
\tag{6}
$$

where $u_{\boldsymbol{\nu}}$ is the solution of the forward problem (1) for inclusions defined by parameters $\boldsymbol{\nu}$. To this purpose, iterative optimization techniques are often employed [26, 44, 45]. In the absence of noise, the parameters characterizing the exact inclusions furnish a global minimum of the deterministic cost $J_d(\boldsymbol{\nu})$. Additional local minima may be present depending on the data quality. The term $R(\boldsymbol{\nu})$ is a regularizing term aiming to convexify the cost and ensure the occurrence of a unique global minimum. Typical choices are Tikhonov and total variation terms [16, 23] but also iteratively regularizing Gauss Newton schemes, in which the regularizing term vanishes while optimizing [34]. The later schemes have the potential of providing solutions which are robust for certain noise levels.

2.3 Bayesian inverse problem

Bayesian approaches aim to quantify uncertainty in the solution of the inverse problem relying on Bayes' formula [38, 55]. In finite dimension, we consider the parameters random as variables with posterior density

$$
p_\mathrm{pt}(\boldsymbol{\nu}) := p(\boldsymbol{\nu}|\mathbf{d}) = \frac{p(\mathbf{d}|\boldsymbol{\nu})}{p(\mathbf{d})} p_\mathrm{pr}(\boldsymbol{\nu}),
\tag{7}
$$

given data $\mathbf{d}$. The prior density $p_{\mathrm{pr}}(\boldsymbol{\nu})$ represents the available prior knowledge whereas the conditional probability $p(\mathbf{d}|\boldsymbol{\nu})$ describes the likelihood of the measurements $\mathbf{d}$ given the parameters $\boldsymbol{\nu}$. The density $p(\mathbf{d})$ is a normalization factor, to keep the integral of the posterior probability equal to one. Here, we choose a likelihood

$$p(\mathbf{d}|\boldsymbol{\nu}) = \frac{1}{(2\pi)^{N/2}\sqrt{|\boldsymbol{\Gamma}_{\mathrm{n}}|}} \exp\left(-\frac{1}{2}\|\mathbf{o}(\boldsymbol{\nu}) - \mathbf{d}\|_{\boldsymbol{\Gamma}_{\mathrm{n}}^{-1}}^2\right), \tag{8}$$

where $\|\mathbf{v}\|_{\boldsymbol{\Gamma}_{\mathrm{n}}^{-1}}^2 = \bar{\mathbf{v}}^t \boldsymbol{\Gamma}_{\mathrm{n}}^{-1} \mathbf{v}$, with t denoting transpose, D is the dimension of $\mathbf{d}$ and $\mathbf{o}(\boldsymbol{\nu})$ represents the observation operator. We consider a diagonal covariance matrix $\boldsymbol{\Gamma}_{\mathrm{n}}$ with constant diagonal of magnitude $\sigma_{\mathrm{noise}}^2$. A typical choice for $p_{\mathrm{pr}}(\boldsymbol{\nu})$ is a multivariate Gaussian with covariance matrix $\boldsymbol{\Gamma}_{\mathrm{pr}}$

$$p_{\mathrm{pr}}(\boldsymbol{\nu}) = \begin{cases} \frac{1}{(2\pi)^{P/2}}\frac{1}{\sqrt{|\boldsymbol{\Gamma}_{\mathrm{pr}}|}} \exp\left(-\frac{1}{2}\|\boldsymbol{\nu} - \boldsymbol{\nu}_0\|_{\boldsymbol{\Gamma}_{\mathrm{pr}}^{-1}}^2\right) & \boldsymbol{\nu} \in \mathcal{P}, \\ 0 & \boldsymbol{\nu} \notin \mathcal{P}, \end{cases} \tag{9}$$

where $\mathcal{P}$ represents a set of constraints to be satisfied by $\boldsymbol{\nu}$. The resulting posterior probability is proportional to

$$p(\boldsymbol{\nu}|\mathbf{d}) \sim \exp\left(-\frac{1}{2}\|\mathbf{o}(\boldsymbol{\nu}) - \mathbf{d}\|_{\boldsymbol{\Gamma}_{\mathrm{n}}^{-1}}^2 - \frac{1}{2}\|\boldsymbol{\nu} - \boldsymbol{\nu}_0\|_{\boldsymbol{\Gamma}_{\mathrm{pr}}^{-1}}^2\right), \quad \boldsymbol{\nu} \in \mathcal{P}. \tag{10}$$

The solution of the inverse Bayesian problem is the characterization of the posterior probability. Full characterization of this unnormalized posterior distribution is a challenging problem that can be addressed by Markov Chain Monte Carlo (MCMC) methods [4, 27] to a certain extent. The most likely set of parameter values $\boldsymbol{\nu}_{\mathrm{MAP}}$ defines the MAP (maximum a posteriori) estimate and minimizes the functional

$$J(\boldsymbol{\nu}) = \frac{1}{2}\|\mathbf{o}(\boldsymbol{\nu}) - \mathbf{d}\|_{\boldsymbol{\Gamma}_{\mathrm{n}}^{-1}}^2 + \frac{1}{2}\|\boldsymbol{\nu} - \boldsymbol{\nu}_0\|_{\boldsymbol{\Gamma}_{\mathrm{pr}}^{-1}}^2, \tag{11}$$

which is expected to be convex for good choices of $\boldsymbol{\nu}_0$ and $\boldsymbol{\Gamma}_{\mathrm{pr}}$, however, the prior information might not be good enough. Compared to (6), the first term is the deterministic cost $J_{\mathrm{d}}(\boldsymbol{\nu})$ scaled by $\sigma_{\mathrm{noise}}^2$, while the second acts as a Bayesian regularizing term $\mathcal{R}(\boldsymbol{\nu})$. Once we have calculated $\boldsymbol{\nu}_{\mathrm{MAP}}$, the so-called Laplace approximation linearizes the posterior distribution about $\boldsymbol{\nu}_{\mathrm{MAP}}$ and estimates the posterior distribution through a multivariate Gaussian distribution $\mathcal{N}(\boldsymbol{\nu}_{\mathrm{MAP}}, \boldsymbol{\Gamma}_{\mathrm{pt}})$ [43, 50]. This may be a useful approximation when the posterior distribution is not multimodal, otherwise it only captures the main mode.

3 Approximate inverse problem

For computational studies, the continuous observation operator (4) must be replaced by a discrete approximation. The accuracy of this approximation depends on the scheme used to construct numerical solutions of (1). In homogeneous backgrounds, and for stationary constraints, boundary value elements furnish an efficient procedure

that minimizes numerical artifacts [9, 32, 34] and computational costs associated to mesh design. In a layered medium and with time dependent constraints, we are forced to rely on finite element methods and face issues related to mesh design and computational cost.

3.1 Truncated forward problem

Due to the finite speed of propagation of waves, the wave field solution of (1) will only be nonzero inside the domain of influence of the emitted waves [37]. One can exploit this fact to truncate the computational domain to a finite rectangular domain. Given a time $\tau > 0$, we can truncate the half-space to a large box R_τ in such a way that the wave field vanishes at its bottom and lateral boundaries during the time interval $[0, \tau]$. Then, the problem set in the whole halfspace is equivalent to the problem set in R_τ with zero Dirichlet or Neumann boundary conditions at those boundaries for $t \in [0, \tau]$. For computational purposes, we often need the computational region to be as small as possible. Under some conditions the original model can be replaced by an equivalent problem set in a smaller rectangle R provided adequate nonreflecting boundary conditions are available. A typical choice for scalar wave equations with constant coefficients are conditions of the form $\frac{\partial u}{\partial \mathbf{n}} = -\frac{u_t}{v_{\mathrm{p}}}$, where v_{p} is the wave speed, see [22]. Similar conditions can be exploited in layered geometries, as depicted in Figure 1. The truncated problem is then

$$
\begin{aligned}
\rho(\mathbf{x})\, u_{tt} &= \operatorname{div}(\chi(\mathbf{x})\nabla u) + \rho(\mathbf{x})h(t,\mathbf{x}), \quad &&\mathbf{x} \in R,\, t \in [0,T], \\
\nabla u \cdot \mathbf{n} &= 0, &&\mathbf{x} \in \Sigma,\, t \in [0,T], \\
\nabla u \cdot \mathbf{n} &= -\gamma(\mathbf{x})u_t, &&\mathbf{x} \in \partial R \setminus \overline{\Sigma},\, t \in [0,T], \\
u(0,\mathbf{x}) &= u_0(\mathbf{x}),\; u_t(0,\mathbf{x}) = u_1(\mathbf{x}), &&\mathbf{x} \in R,
\end{aligned}
\tag{12}
$$

where ρ and χ are defined in (2) and (3) and $\gamma = \rho v_{\mathrm{p}}$. Existence of solutions to this problem when $\gamma > 0$ is not immediate, since the boundary condition uses values of u_t on the boundary. Standard existence results for wave equations guarantee the existence of solutions with $L^2(R)$ derivatives u_t. However, for u_t to have a trace on ∂R we would need at least $H^1(R)$ regularity. Appendix B establishes existence, uniqueness, regularity and stability results for (12). When $\gamma = 0$, we have a standard Neumann problem.

3.2 Choice of mesh and discretization

Problem (12) is set in layered domains with inclusions represented by piecewise constant coefficients. Domain decomposition techniques [3] provide effective tools to address it. For this purpose, the spatial mesh must adapt to the interfaces: all the triangles must be entirely contained in one subdomain and connecting triangles share vertices lying on the boundaries between domains, see Figure 2(a). Studying the posterior distribution (10) by MCMC techniques requires solving millions of forward problems with different subdomains, as defined by different $\boldsymbol{\nu}$ choices. Domain decomposition techniques require new meshes for each choice of $\boldsymbol{\nu}$ and become unaffordable,

8

forcing the use of rougher approximations built on fixed meshes, see Figure 2 (b) and (c). In contrast, optimization problems (6) and (11) can be addressed with either adaptive or fixed meshes, which allows us to evaluate the effect of using different meshes, while keeping the same discretization schemes.

For a given mesh, Appendix C describes the discretization procedure we have employed in the tests performed here, as well as their approximation properties. Figure 2 compares the effect of the triangulation choices on the numerically observed data at the receivers. The largest errors are observed when comparing results obtained with the adapted and uniform meshes, while the smallest errors correspond to comparison of results calculated with the adapted and stratified mesh (adapted to the layers, but not to the inclusion). As the maximum diameter of the triangulation elements δx tends to zero, we can prove convergence for adapted meshes, see Appendix C. A better approximation of the transmission conditions for wave propagation at the interface between subdomains is expected.
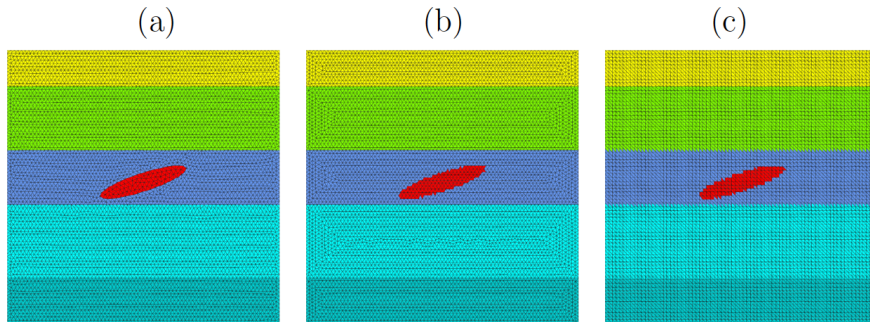

Figure 2: Types of meshes considered: (a) adapted to all the subdomains, (b) adapted to the stratified structure but not to the changing inclusion, (c) uniform.

The numerical tests presented in this paper use synthetic data generated employed either of the three meshes and corrupted by noise up to a 15% level to solve a nondimensionalized version (18) of (12), see Appendix A for details and typical parameter choices.

3.3 Approximate observation operators and discrete Bayesian formulation

For computational studies, the original problem is replaced by a discretized version that employs approximate observation operators $\mathbf{o}_{\mathrm{ap}}$

$$
\begin{aligned}
\mathbf{o}_{\mathrm{ap}} : \quad & \mathbb{R}^P \longrightarrow \mathbb{R}^D \\
& \boldsymbol{\nu} \longrightarrow (u_{\boldsymbol{\nu},\mathrm{ap}}(\mathbf{r}_j, t_m))_{j=1,\dots,J, m=1,\dots,M},
\end{aligned}
\tag{13}
$$

where $u_{\boldsymbol{\nu},\mathrm{ap}}$ is the approximation to the solution of (1) generated by solving numerically (18) with the selected schemes.
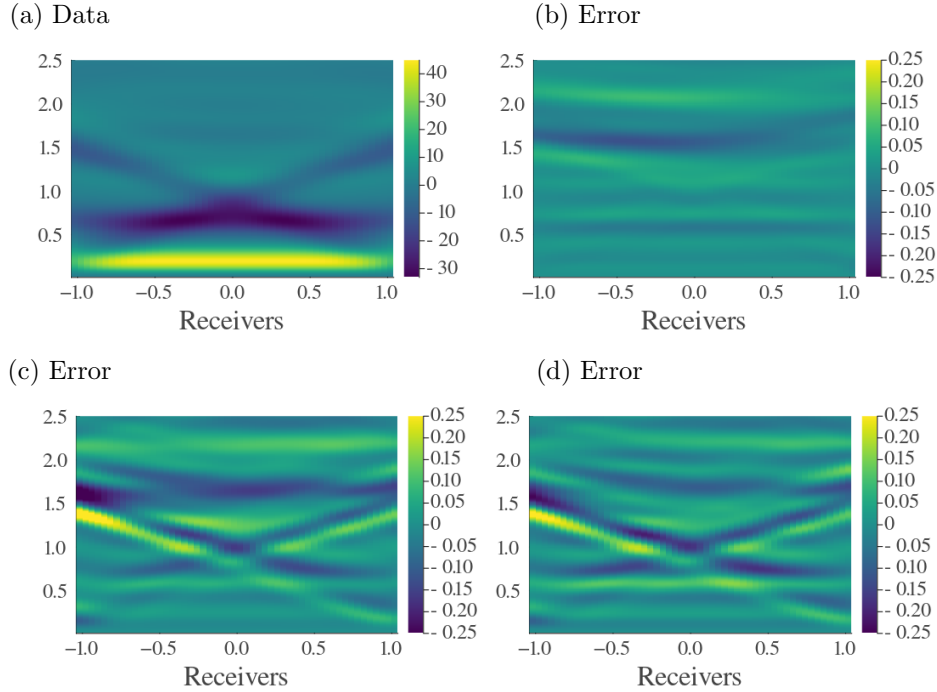
(a) Data

(b) Error

(c) Error

(d) Error

Figure 3:   (a) Values recorded at the receivers with the adaptive mesh in Figure 2(a) for the parameter values and geometry in Figure 1 with $\delta x = 0.04$, $\delta t = $ 1e-3. Profiles are recorded at intervals of 0.01. Errors when comparing the data in (a) with the observed values obtained with (b) the stratified mesh in Figure 2(b) and (c) the uniform mesh in Figure 2(c) and when comparing the data obtained with the latter two meshes between themselves (d).

Here, we will use the scheme (43) described in Appendix C with three different mesh choices: adapted, stratified and uniform. The latter two lead to two different and fixed approximate observation operators during the whole optimization and sampling procedures, which we denote $\mathbf{o}_{ap_s}$, and $\mathbf{o}_{ap_u}$, respectively. The posterior distribution to be explored becomes

$$p(\boldsymbol{\nu}|\mathbf{d}) \sim \exp\left(-\frac{1}{2}\|\mathbf{o}_{\text{ap}}(\boldsymbol{\nu}) - \mathbf{d}\|^2_{\boldsymbol{\Gamma}_n^{-1}} - \frac{1}{2}\|\boldsymbol{\nu} - \boldsymbol{\nu}_0\|^2_{\boldsymbol{\Gamma}_{\text{pr}}^{-1}}\right), \tag{14}$$

whereas the cost to be optimized to evaluate the MAP estimate is

$$J(\boldsymbol{\nu}) = \frac{1}{2}\|\mathbf{o}_{\text{ap}}(\boldsymbol{\nu}) - \mathbf{d}\|^2_{\boldsymbol{\Gamma}_n^{-1}} + \frac{1}{2}\|\boldsymbol{\nu} - \boldsymbol{\nu}_0\|^2_{\boldsymbol{\Gamma}_{\text{pr}}^{-1}}. \tag{15}$$

Compared to the original distributions (10) and costs (11) the difference $\mathbf{o}(\boldsymbol{\nu}) - \mathbf{o}_{\text{ap}}(\boldsymbol{\nu})$ could result in variations in the original landscape of high probability configurations (resp. local minima), specially when the mesh is kept fixed. Instead, the use of

10

meshes that adapt to inclusions as they vary results in continuous changes in the approximate observation operator in an attempt to reproduce better the original observation operator.

Next, we introduce techniques to numerically approximate the MAP points.

4 Calculation of maximum a posteriori estimates

To approximate the highest probability parameter sets which minimize the cost functionals (11) or (15), we adapt techniques of deterministic optimization [45] (more precisely, Levenberg-Marquardt-Fletcher type approaches [26]) and also Markov Chain Monte Carlo methods. A delicate point in the implementation of optimization schemes is the approximation of the derivatives of solutions u_ν of (12) with respect to ν, which requires either a characterization of such derivatives as the solution of an auxiliary problem or adequate numerical schemes depending on the selected type of mesh. We introduce next an automatic strategy to minimize functional (11) employing adaptive meshes and an strategy to locate possible additional minima resorting to fixed meshes. In principle, we can locate additional minima by means of affine invariant MCMC samplers [28] too. MCMC methods are technically easier to implement, since only forward solvers are needed. However, the number of auxiliary problems to be solved increases from a few tens to a few hundred thousand or millions.

4.1 Iterative optimization scheme for adaptive meshes

We choose the prior mean ν_0 as initial guess of the parametrization, $\nu^0 = \nu_0$ and implement the Newton type iteration $\nu^{k+1} = \nu^k + \xi^{k+1}$ where ξ^{k+1} is the solution of

$$\left(\mathbf{H}(\nu^k) + \omega_k \mathrm{diag}(\mathbf{H}(\nu^k))\right)\xi^{k+1} = -\mathbf{g}(\nu^k) \tag{16}$$

Here, $\mathbf{H}(\nu)$ and $\mathbf{g}(\nu)$ represent the Hessian and the gradient of the selected cost, that involve first and second order derivatives of the solutions of the forward problems with respect to ν. Since we are only interested in seeking descent directions, in practice, we replace $\mathbf{H}(\nu)$ by the Gauss-Newton part of the Hessian $\mathbf{H}^{\mathrm{GN}}(\nu)$ neglecting second order derivatives. The small parameter $\omega_k > 0$ is adjusted to guarantee a decrease in the cost. We reduce it as the cost $J(\nu^k)$ decreases and we increase it if the proposed ξ^{k+1} leads to a gain in the cost [44, 26].

In the adaptive approach we propose, we recalculate the mesh and triangulation of the computational region R any time we update the inclusion parametrization ν^k in (43)-(44) with ρ, χ, v_{p} defined in (2)-(3) and $\gamma = \chi/v_{\mathrm{p}}$. We adapt the finite element mesh to the shape of the domains in which the physical properties take different constant values using a technique developed by Gilbert Strang and Per-Olof Persson in [48, 49]. Then, u_{ν^k} is calculated by means of (43)-(44). At each step, we approximate the derivatives of the solutions u_{ν^k} with respect to ν by means of algorithmic differentiation [52]. The process stops when either the difference between parameterizations or the cost value fall below given tolerances. The final value provides an approximation to ν_{MAP}.

The algorithm steps can be summarized as follows, see [46] for implementation details:

- *Initialization:* Define

    - prior mean $\boldsymbol{\nu}_0$ (inclusion shape and material parameters) and prior covariance $\mathbf{\Gamma}_{\mathrm{pr}}$,
    - measured data $\mathbf{d}$ and noise level σ_{noise},
    - emitter grid $\mathbf{x}_k$, $k = 1, \ldots, K$, receiver grid $\mathbf{r}_j$, $j = 1, \ldots, J$, recording times t_m, $m = 0, \ldots, M$,
    - material parameters for ρ and v_{p} on the layered structure and emitted signal $f(t)G(\mathbf{x})$,
    - maximum number of optimization steps S, spatio-temporal steps δt, δx and δy for the solver, final time T and tolerances.

    Set the initial parameterization $\boldsymbol{\nu}^0$ equal to the prior mean.

- *Optimization:* From $i = 1$ to S

    - Build a triangulation $\mathcal{T}^i$ adapted to the current geometry of the inclusions and the underlying layered structure (ie. each triangle is fully contained in a subdomain with constant coefficients):
        * Implement the Persson-Strang method [48, 49].
        * Store the resulting points and triangulation.
    - Solve numerically the boundary value problem (18):
        * Construct a space of linear finite elements on the adapted triangulation $\mathcal{T}^i$, designed to admit forward automatic differentiation with respect to points, triangulation and elastic parameters.
        * Update the FEM matrices (44) to reflect the coefficient values for the current inclusion.
        * Implement the variant of the discretization scheme (43) for (41).
        * Evaluate the numerical solution $u_{\boldsymbol{\nu}^i}$ at the receivers to calculate the observation operator $\mathbf{o}_{\mathrm{ap}}(\boldsymbol{\nu}^i)$.
    - Solve system (16) to calculate $\boldsymbol{\nu}^{i+1}$:
        * Approximate the variation of the solutions $u_{\boldsymbol{\nu}^i}$ at the receivers with respect to $\boldsymbol{\nu}$ by means of algorithmic differentiation [52] to obtain $\mathbf{H}(\boldsymbol{\nu}^i)$ and $\mathbf{g}(\dot{\boldsymbol{\nu}}^i)$.
        * Propose a descent direction $\boldsymbol{\xi}^{i+1}$ using (16) and evaluate the cost $J(\boldsymbol{\nu}^{i+1})$ given by (15) with $\boldsymbol{\nu}^{i+1} = \boldsymbol{\nu}^i + \boldsymbol{\xi}^{i+1}$.
        * If $J(\boldsymbol{\nu}^{i+1}) < J(\boldsymbol{\nu}^i)$ accept $\boldsymbol{\nu}^{i+1}$, set $\omega^{i+1} = \omega^{i+1}/2$ and move to the next optimization step. Otherwise, divide ω^i by 2 and repeat until satisfied.
        * If either $\|\boldsymbol{\nu}^{i+1} - \boldsymbol{\nu}^i\|$ or $J(\boldsymbol{\nu}^{i+1})$ fall below specified tolerances, stop.

- *Output:* Optimal inclusion shape and material parameters defining $\boldsymbol{\nu}_{\mathrm{MAP}}$, gradient and Hessian of the cost at $\boldsymbol{\nu}_{\mathrm{MAP}}$, as well as intermediate $\boldsymbol{\nu}^i$ and $J(\boldsymbol{\nu}^i)$ values.

This algorithm can be coded in Julia to exploit specific meshing and automatic differentiation packages. The resulting adaptive scheme is fully automatic: the user must only provide the data and the parameters defining the cost functional, that is, the prior knowledge, and the level of noise. Meshes are automatically adapted to the new object and internal variables for the calculation of derivatives and the advance of iterations are adjusted automatically. The user must only provide the data and the parameters defining the cost functional, that is, the prior knowledge, and the level of noise.

On a laptop, building an adapted triangulation takes about 31 seconds and solving one forward problem takes about 29 seconds. One iteration of the optimization routine takes about 14 minutes (it may involve several object proposals and triangulations). The usual 20 steps make take about 4 hours. This process is not paralellized due to the difficulty of parallelizing mesh generation.

Figures 4-6 summarize results for the true configuration represented in Figure 1 for increasing noise levels in the data. Synthetic data for different noise levels r are generated an explained in Appendix A. Figures 4 and 5 illustrate the evolution of the inclusion geometry and its material properties along the optimization procedure for 10% noise. The object can move from one layer to another, shrink and expand or rotate as its material properties change. Table 1 contains the parameter values for the true inclusion and the initial approximation, as well as the MAP estimate obtained optimizing (11) for 5% and 15% noise. Figure 4 visualizes the true object, the prior and the final estimate provided by the optimization procedure. Inclusions are defined by the parameters $\boldsymbol{\nu} = (c_{\mathrm{x}}, c_{\mathrm{y}}, a, b, \theta, \rho, v_{\mathrm{p}})$, that its, center, semi-axes, angle with the positive x-axis, density and wave speed. We choose as prior means for ρ and v_{p} the average of the maximum and minimum values available for the layers, that is, $(\rho_{\max} + \rho_{\min})/2$ and $(v_{\mathrm{p},\max} + v_{\mathrm{p},\min})/2$. Then, the standard deviations σ_ρ and σ_{v_p} are taken equal to half the difference between the maximum and minimum values in the whole sequence of known layers, that is, $\sigma_\rho = (\rho_{\max} - \rho_{\min})/2$ and $\sigma_{v_{\mathrm{p}}} = (v_{\mathrm{p},\max} - v_{\mathrm{p},\min})/2$. For the tests presented here we have set in the cost $\boldsymbol{\Gamma}_{\mathrm{pr}} =$ diag $(1, 1, 0.5, 0.5, 0.1, \sigma_\rho^2, \sigma_{v_{\mathrm{p}}}^2)$ and $\boldsymbol{\Gamma}_{\mathrm{n}} = \sigma_{\mathrm{noise}}^2 \mathbf{I}$, $\sigma_{\mathrm{noise}} = \sigma\, r/100$, σ being the normalized ℓ^2 norm of the true data (see Appendix A).

In the tests we have performed, this automatic algorithm leads to similar results for rotated inclusions (clockwise or anti-clockwise) even if we place the prior in a different layer or if the true object lies between different layers. Keeping the same material parameters, the MAP estimates for the geometry of rotated inclusions in this set-up remain quite close to the true shape, as well as the density, while the velocity varies a bit more. Remarkably, the prediction for horizontal inclusions may depart from the true shape as we vary the prior, see Figure 7, obtained for different initial curves with the same material parameters. Notice that changing the prior we change the continuous functional to be optimized. Later MCMC studies will clarify this observation, see Figure 8(d).
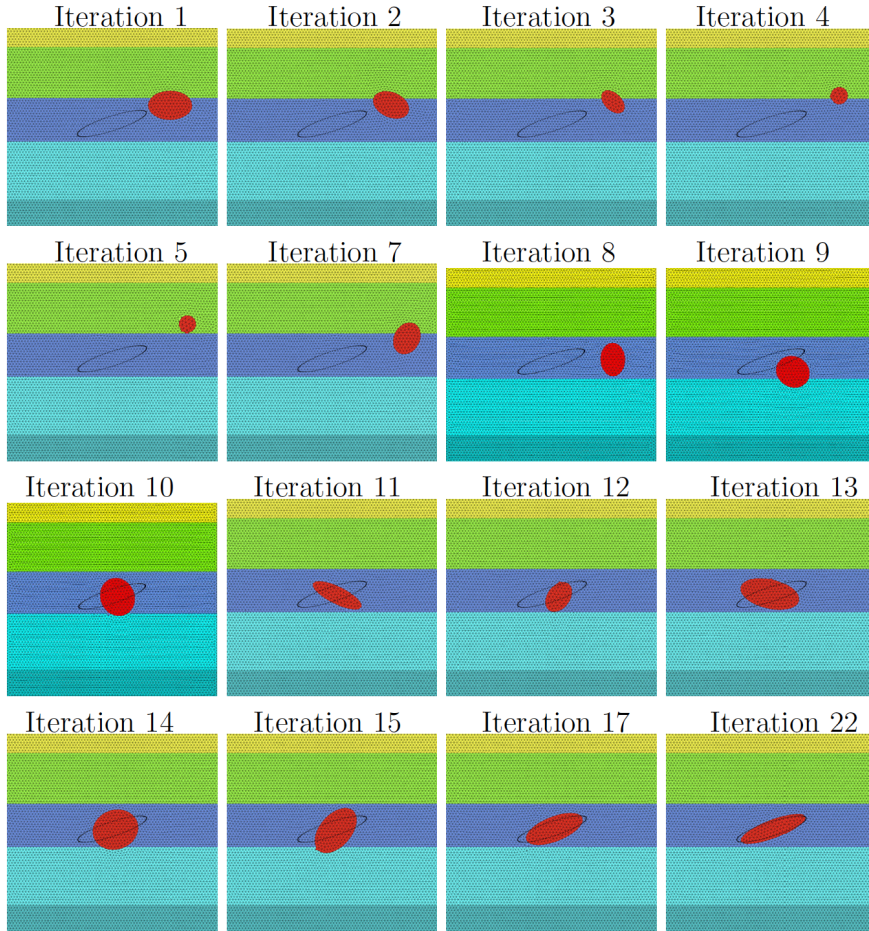
13

Figure 4: True inclusion (black curve) compared to the shapes obtained at successive iterations (red) for 10% noise during adaptive constrained optimization.

4.2 Iterative optimization scheme for fixed meshes

When working with prefixed meshes, we implement the previous scheme with four differences.

First, we construct the mesh at the start, and keep it unchanged during the optimization process. The observation operator is thus (13) with $\mathbf{o}_{\mathrm{ap_s}}$ or $\mathbf{o}_{\mathrm{ap_u}}$, and the cost (15). Thanks to the structure of the scheme (43), all the matrices can be calculated for a configuration without inclusions and stored at the start of the process. Whenever we propose an inclusion, only the coefficients corresponding to nodes involving it are updated. The resulting matrices are kept fixed to calculate the approximate solution $u_{\boldsymbol{\nu}^k,\mathrm{ap}}$ of the corresponding problem and the required observed data. Matlab routines to construct FEM matrices allow to locate the affected nodes,
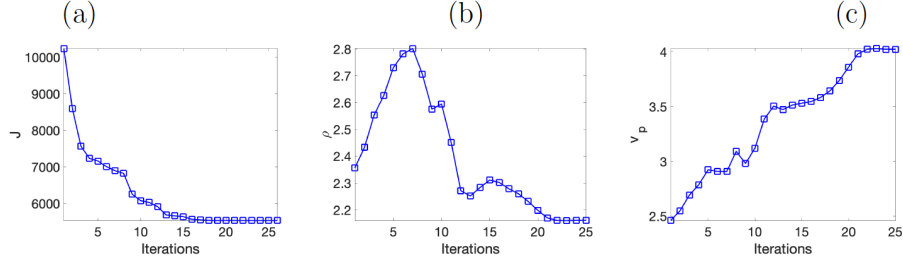
14

Figure 5: Evolution of (a) the cost, (b) ρ and (c) v_p inside the inclusion along the iterations for the simulation in Figure 5.

Parameter	True	Prior	Adaptive 5%	Adaptive 15%
x center	0.0	0.5	0.0110207	0.030625
y center	-1.45	-1.4	-1.44922	-1.446588
semi-major axis	0.5	0.3	0.485523	0.472986
semi-minor axis	0.1	0.2	0.113252	0.1305437
rotation angle	0.314159	0.0	0.340005	0.38868
density	2.1	2.3	2.13201	2.182858
velocity	4.4	2.4	4.17327	3.9267512

Table 1: Dimensionless inclusion parameters compared to the parameters defining the initial approximation and the final MAP estimate obtained by adaptive constrained optimization for different noise levels.

enabling us to perform this process quite fast.

Second, to estimate the change of the solution $u_{\boldsymbol{\nu},\mathrm{ap}}$ when varying the parameters ν_i, we rely on difference approximations [11].

$$\frac{\partial u_{\boldsymbol{\nu},\mathrm{ap}}}{\partial \nu_i}(\mathbf{r}_k, t_m) \sim \frac{u_{\boldsymbol{\nu}+\eta_i,\mathrm{ap}}(\mathbf{r}_k, t_m) - u_{\boldsymbol{\nu},\mathrm{ap}}(r_k, 0, t_m)}{\eta_i},$$

with η_i small, $u_{\boldsymbol{\nu}+\eta_i,\mathrm{ap}}$ being the numerical solution of the forward problem with ν_i replaced by $\nu_i + \eta_i$. Notice that we do not need detailed derivative studies. We just use these quotients to generate descent directions for the cost.

Third, to calibrate the steps η_i in these approximations we have swept a grid of small values, that are selected and then kept fixed for all approximations during the iterations performed in the optimization procedure.

Four, this strategy results in iterative procedures that decrease the initial value of the cost and stop when changes in the cost or parameters fall below given tolerances. While varying the parameter η, the scheme may converge to different parameter sets $\boldsymbol{\nu}$ with different cost values. The set yielding the minimum value of the cost is selected as $\boldsymbol{\nu}_{\mathrm{MAP}}$.

For the data considered in Section 4.1, Table 2 collects the results obtained for $\boldsymbol{\nu}_{\mathrm{MAP}}$ employing fixed uniform meshes with observation operator $\mathbf{o}_{\mathrm{ap}_u}$. Similar results are
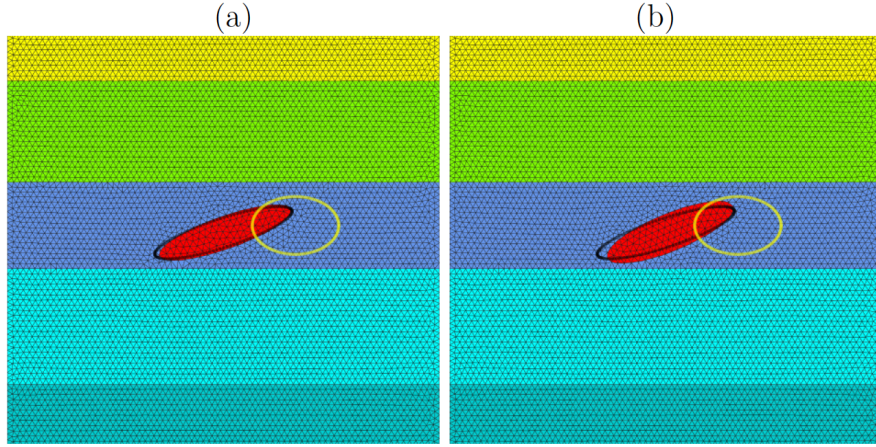
Figure 6: True inclusion (black curve) compared to the initial (prior) configuration (yellow curve) and the MAP estimate of the shape (meshed in red) after convergence of adaptive constrained optimization in (a) 28 iterations for 5% noise, (b) 29 iterations for 15% noise. MAP values are given in Table 1.
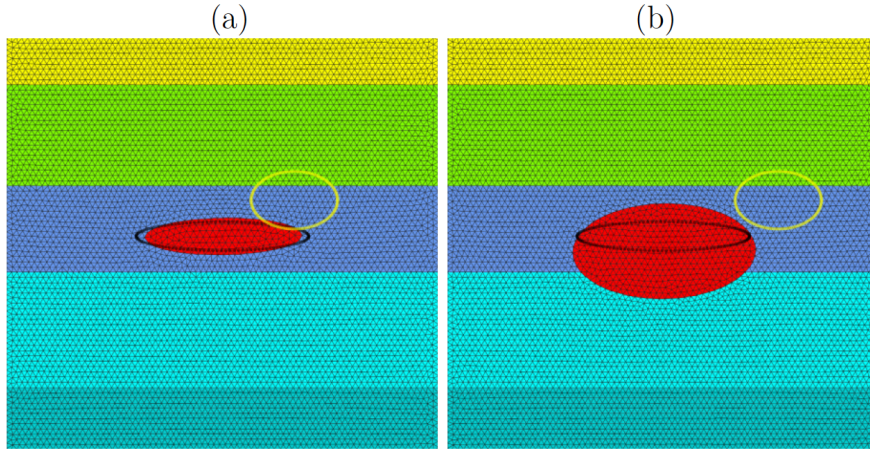

Figure 7: MAP estimates of the shape of an horizontal inclusion obtained by adaptive constrained optimization with slightly different prior shapes for 10% noise. The MAP estimates of ρ and v_p are 2.13 and 4.03 for (a) and 2.32 and 3.96 for (b).

found for $\mathbf{o}_{\mathrm{ap}_s}$. In both cases, the optimization algorithm provides other configurations with slightly higher cost as we sweep the grid for η, which suggests the presence of secondary local minima, since the prior and the mesh are kept fixed now. Nevertheless, most choices of η lead to $\boldsymbol{\nu}_{\mathrm{MAP}}$. Compared to the adaptive algorithm, carrying out this

16

process on a laptop for a single value of η takes a few minutes, when coded in Matlab and conveniently parallelized. For the grids we are considering, with maximum steps 0.04 in x and y, it takes about 1.5-3 minutes to converge for a uniform mesh and between 14 and 94 minutes for a stratified mesh. Switching to maximum step 0.06 in the x direction, time goes down to 4-14 minutes for the stratified mesh. Sweeping a grid of values of η to search for other possible local minima increases the cost: about 20 minutes for the uniform mesh and about 5 hours or 1 hour for the stratified mesh. This requires checking local convergence to asses whether the stopping point is a possible local minimum or the iterations stops because the descent strategy does not produce suitable descent directions. As said before, the adaptive algorithm is more difficult to parallelize and it may take a few hours on a laptop without parallelization. However, it is fully automatic.

Parameter	Fixed 5%	Fixed 15%	MCMC 5%	MCMC 15%
x center	0.01766	0.040319	0.0217	0.0052
y center	-1.4489	-1.448	-1.4476	-1.4548
semi-major axis	0.4844	0.4766	0.4856	0.4588
semi-minor axis	0.10071	0.13516	0.0940	0.1379
rotation angle	0.3264	0.3474	0.3334	0.3175
density	2.0977	2.1991	2.0718	2.1457
velocity	4.3678	3.8257	4.4645	3.9275

Table 2: Counterpart of Table 3 for constrained optimization and MCMC schemes using fixed uniform meshes.

4.3 Optimization by Markov Chain Monte Carlo methods

A Markov chain is a sequence of events for which the probability of an event depends only on the event just before it. To define a Markov Chain we need three elements [27]: the space of states X, that is, the set of values the chain can take, the transition operator $q(x^{k+1}|x^k)$, which defines the probability of transitioning from state x^k to state x^{k+1}, and the initial distribution π, which defines the probability of being in any one of the possible states at the start, for $k = 0$. To generate a Markov chain $x^0 \rightarrow x^1 \rightarrow x^2 \ldots \rightarrow x^k \rightarrow \ldots$ we sample the initial state x^0 from π and transition from x^k to x^{k+1} according to $q(x^{k+1}|x^k)$, $k \geq 0$.

Markov chains satisfying a number of properties (time homogeneity, detailed balance) are shown to equilibrate to target distributions p under some conditions [43, 27]. Different strategies to construct Markov Chains enjoying these properties have been proposed. We choose here the affine invariant ensemble sampler developed in [28], that can handle multimodal distributions and allows for parallelization [10]. The idea is to create W chains that are mixed at each step: [28]:

- Set the number of chains W, the number of steps S and choose $a \sim 2$.

- Set the sample space $X = \mathbb{R}^P$, P dimension of the parameter space.

- Draw $\boldsymbol{\nu}_1^0, \ldots, \boldsymbol{\nu}_W^0$ in X with probability p_{pr}.

- From $k = 0$ to $k = S$:

    – Generate a permutation σ of $(1, \ldots, P)$ without fixed elements.
    – For $w = 1, \ldots, W$
        * Draw z_w from $g(s) = s^{-1/2}$ if $s \in [a^{-1}, a]$, 0 otherwise.
        * Set $\boldsymbol{\nu}_{\mathrm{prop},w} = \boldsymbol{\nu}_{\sigma(w)}^k + z_w(\boldsymbol{\nu}_w^k - \boldsymbol{\nu}_{\sigma(w)}^k)$.
        * Calculate the acceptance rate $\alpha = \min\left(1, z_w^{P-1} \frac{p_{\mathrm{pt}}(\boldsymbol{\nu}_{\mathrm{prop},w})}{p_{\mathrm{pt}}(\boldsymbol{\nu}_w^k)}\right)$.
        * Draw u with uniform probability $U(0,1)$. If $u < \alpha$, $\boldsymbol{\nu}_w^{k+1} = \boldsymbol{\nu}_{\mathrm{prop},w}$, otherwise $\boldsymbol{\nu}_w^{k+1} = \boldsymbol{\nu}_w^k$.

Discarding an initial transient stage formed by B samples on account of chain equilibration, the remaining states $\boldsymbol{\nu}_w^k$ the chain takes sample from the probability p_{pt}. Notice that we can sample unnormalized distribution like (10) because the normalization factors scale out. This algorithm needs $W > 2P$ to properly sample the target posterior distribution.

Due to the high computational cost of recalculating meshes and auxiliary matrices for each parameter proposal, we employ this method to sample $p_{\mathrm{pt,ap}}$ given by (14) for observation operators $\mathbf{o}_{\mathrm{ap}}$ defined on fixed meshes, that is, $\mathbf{o}_{\mathrm{ap_s}}$ and $\mathbf{o}_{\mathrm{ap_u}}$. The MAP estimate $\boldsymbol{\nu}_{\mathrm{MAP}}$ is the sample for which the probability is higher, that is, the cost $J(\boldsymbol{\nu}) = -\log(p_{\mathrm{pt,ap}}((\boldsymbol{\nu})))$ is minimum.

Table 2 collects the parameters obtained for $\boldsymbol{\nu}_{\mathrm{MAP}}$ for the test case in Figure 1 employing fixed uniform meshes and keeping the data used in the previous two sections. The MAP estimates are similar in the three cases. Figure 8 illustrates additional high probability configurations obtained in this way, as suggested by the sample concentration. Panel (c) suggests that the increased signal to noise ratio associated to a more reflective bottom layer reduces uncertainty. We discuss this point further in the next section.

5   Uncertainty quantification in the object based full-waveform inversion problem

Maximum a posteriori estimates provide a prediction of the most likely values for the inclusion. More precise uncertainty studies provide estimates of the expected range of variation of the different parameters and derived magnitudes.

5.1   Uncertainty quantification based on the Laplace approximation

The Laplace approximation linearizes (14) about $\boldsymbol{\nu}_{\mathrm{MAP}}$ and approximates it by a multivariate Gaussian distribution $\mathcal{N}(\boldsymbol{\nu}_{\mathrm{MAP}}, \boldsymbol{\Gamma}_{\mathrm{pt}})$ The approximate posterior covariance is

$$\boldsymbol{\Gamma}_{\mathrm{pt}} = \mathbf{H}(\boldsymbol{\nu}_{\mathrm{MAP}})^{-1} \sim (\mathbf{F}(\boldsymbol{\nu}_{\mathrm{MAP}})^t \boldsymbol{\Gamma}_{\mathrm{n}}^{-1} \mathbf{F}(\boldsymbol{\nu}_{\mathrm{MAP}}) + \boldsymbol{\Gamma}_{\mathrm{pr}}^{-1})^{-1} = \mathbf{H}^{\mathrm{GN}}(\boldsymbol{\nu}_{\mathrm{MAP}})^{-1},$$
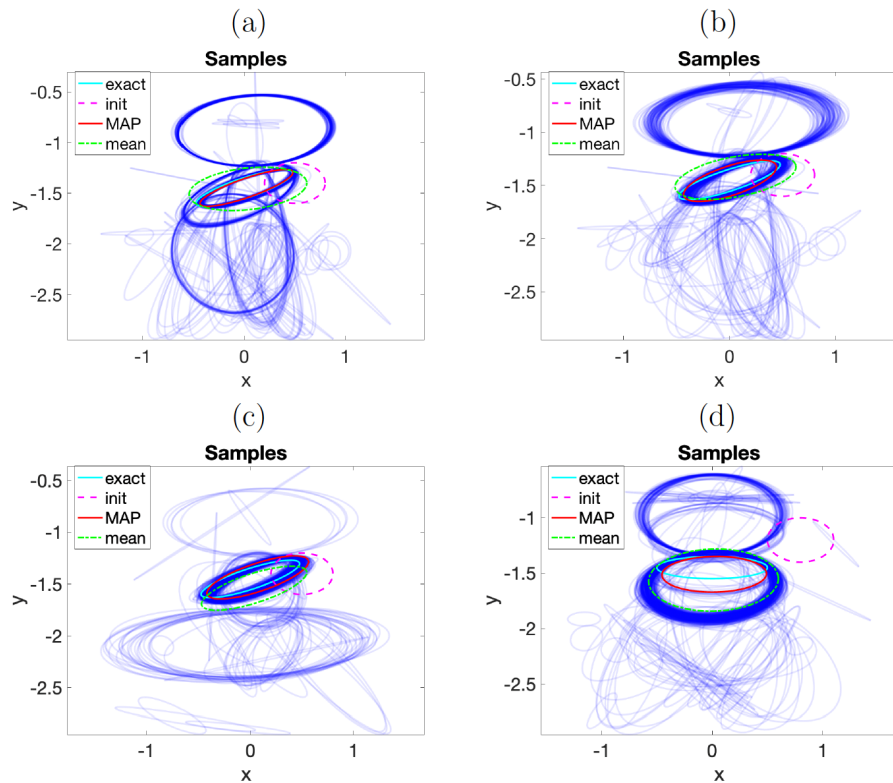
Figure 8: Last W samples for (a) 5% noise, (b) 15% noise, (c) 15% noise with a bottom layer of density $\rho = 2.1$ and larger velocity $v_\mathrm{p} = 4.4$, (d) 10% noise with horizontal inclusion. Parameter values $W = 480$, $a = 2$, $K = 1000$.

where $\mathbf{H}^{\mathrm{GN}}(\boldsymbol{\nu}_{\mathrm{MAP}})$ represents the Gauss-Newton part of the Hessian $\mathbf{H}(\boldsymbol{\nu}_{\mathrm{MAP}})$, which neglects second order derivatives, and $\mathbf{F}(\boldsymbol{\nu}_{\mathrm{MAP}}) = \left(\frac{\partial u_{\boldsymbol{\nu}_{\mathrm{MAP}}}}{\partial \nu_i}(p_k) \right)_{k,i}$ with

$$\mathbf{p} = ((\mathbf{r}_1, t_1), \ldots, (\mathbf{r}_J, t_1), \ldots, (\mathbf{r}_1, t_M), \ldots, (\mathbf{r}_J, t_M)).$$

Samples of the Gaussian approximation $\mathcal{N}(\boldsymbol{\nu}_{\mathrm{MAP}}, \boldsymbol{\Gamma}_{\mathrm{pt}})$ are generated as

$$\boldsymbol{\nu} = \boldsymbol{\nu}_{\mathrm{MAP}} + \boldsymbol{\Gamma}_{\mathrm{pt}}^{1/2}\mathbf{w}, \tag{17}$$

$\mathbf{w}$ being a standard iid vector.

Figures 9-10 visualize the information we obtain about the uncertainty ranges in our predictions for the test case considered in Section 4.1, based on 10.000 samples. We compare the true values, the initial values, the MAP estimate and superimpose histograms built sampling the Laplace approximation of a the posterior distribution (17) with a pdf normalization. These figures use the outcome of the automatic calculations performed with the adaptive optimization scheme in Section 4.1.
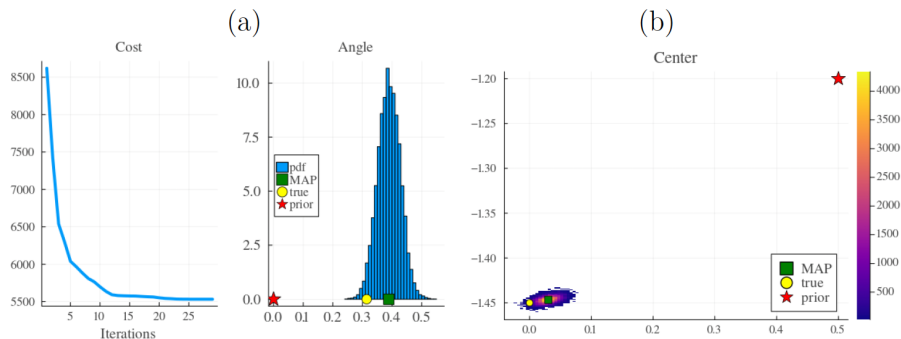
Figure 9: For Figure 6(b) with 15% noise: (a) Cost evolution during MAP calculation by adaptive optimization and uncertainty in angle orientation. (b) Uncertainty in the center position.
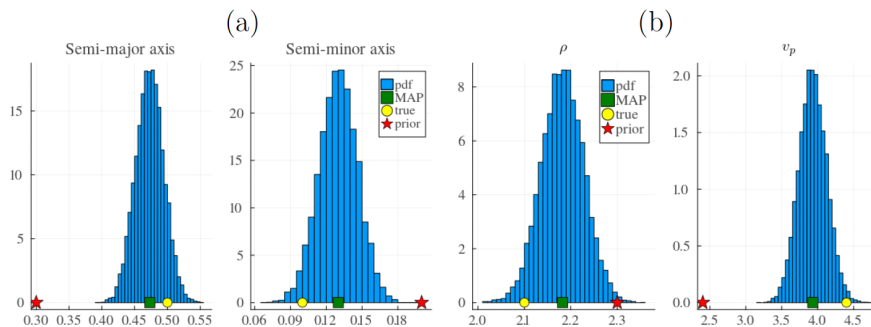

Figure 10: For Figure 6(b) with 15% noise: Uncertainty in (a) the semi axes estimate and (b) the material parameters.

The scheme in Section 4.2 produces similar results for $\boldsymbol{\nu}_{\mathrm{MAP}}$, but suggests the presence of additional local minima representing additional high probability configurations. The posterior probability for the discretized observation operator (13) might be a multimodal distribution with additional peaks. Notice that this approach uses an approximation of the observation operator based on fixed meshes, see remarks in Appendix C, keeping the same data.

5.2 Uncertainty quantification based on MCMC studies

More detailed information on uncertainty on parameter ranges and derived magnitudes is extracted from the analysis of the samples provided by the MCMC chains.

Figure 8(a)-(b) display sets of samples of the posterior distribution (14) with observation operator (13) defined on a fixed uniform mesh for the data used in Figure 4. The MAP estimates for the object geometry and its material properties are now
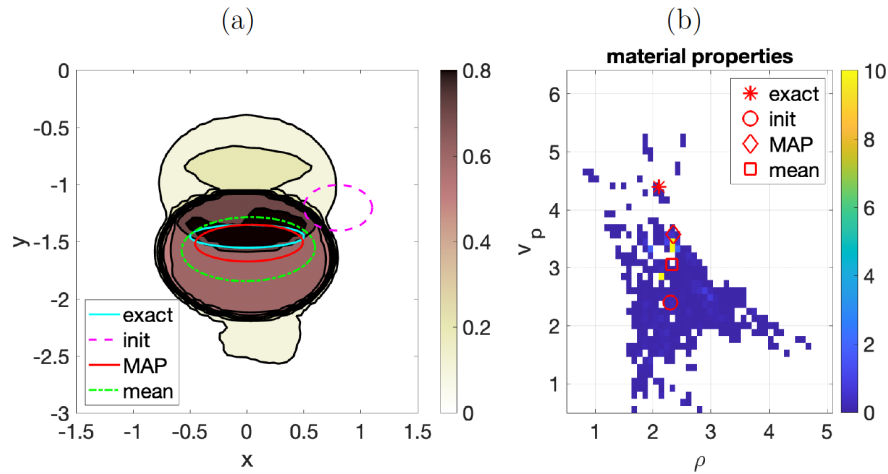
Figure 11: (a) Contour plot of the probability of belonging to the inclusion and (b) projection of the histogram for its material properties (pdf normalization) calculated by MCMC sampling and corresponding to Figure 8(d) with 10% noise.
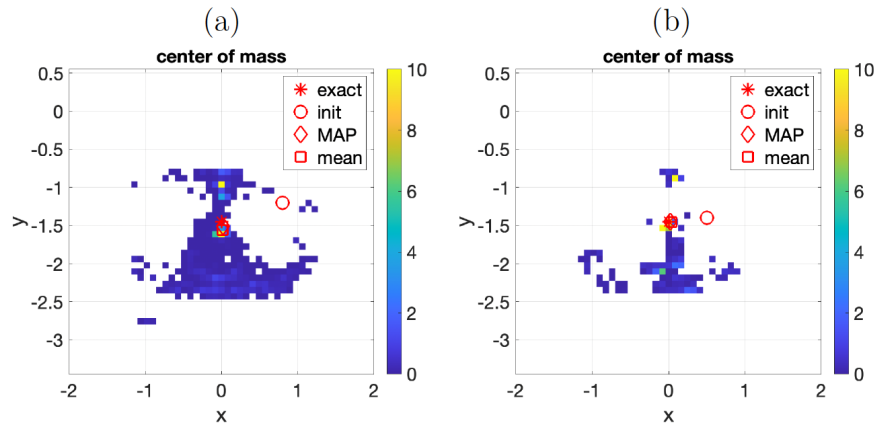

Figure 12: Histograms (pdf normalization) for the centers of mass calculated by MCMC sampling: (a) corresponding to Figure 11, (b) corresponding to Figure 13.

provided by the sample with the highest probability. They are similar to the estimates obtained by optimization with either adaptive or fixed meshes in Section 4. We identify several families of samples in this figure. One wraps around the MAP estimate and the true object. Other are similar to the local minima obtained with the algorithm in Section 4.2 on fixed meshes. The persistence of families of samples with different shape and material properties, as well as the fact that their mean departs from the MAP estimate suggest a multimodal posterior distribution. Increasing the
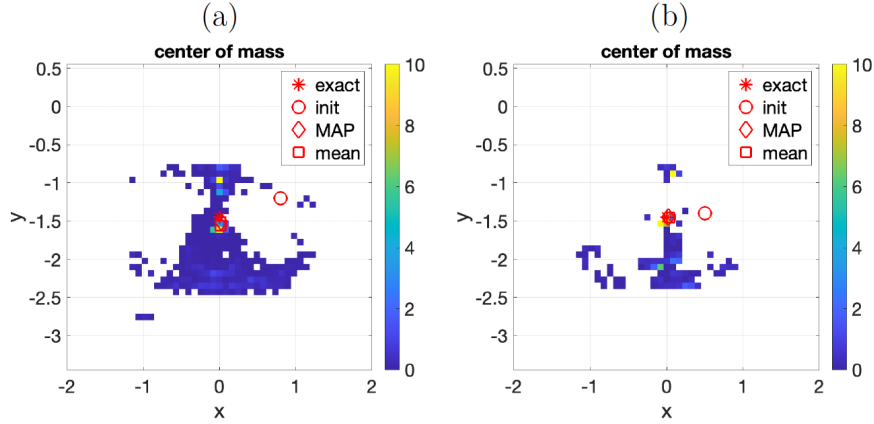
21

Figure 13: (a) Contour plot of the probability of belonging to the inclusion and (b) projection of the histogram for its material properties (pdf normalization) calculated by MCMC sampling and corresponding to Figure 8(a) with 5% noise.

signal to noise ratio by modifying the properties of the bottom layer we observe that multimodality features diminish, see panel (c).

Panel (d) in Figure 8 corresponds to a different inclusion and initial configuration. In this case, the dominant family of samples does not wrap around the MAP and the true object. This suggests that the prior information considered is not enough, neither to convexify the cost, nor to properly approach the true object. This provides some insight on the optimization results in Figure 7: the adaptive scheme evolves towards the dominant mode, closer to the mean, because it has a larger basin of attraction. The scheme in Section 4.2 is able to locate the MAP estimate provided by MCMC sampling. Notice that both employ fixed meshes and consider the same discretized observation operators and cost, whereas the adaptive optimization scheme considers a different approximation operator, thus a different cost functional. Figure 11(a) represents the contour plot of the posterior probability of a point belonging to this object. Panel 12(b) and panel (a) in Figure 12 are projections of histograms representing joint material properties and the center of the inclusion, respectively. Two mains narrow peaks are identified in both, suggesting a bimodal distribution.

Figure 13 revisits the geometry in Figure 1 with the 5% noise data considered in Section 4. Panel (b) for the material properties and panel (b) in Figure 12 for the centers suggest the presence of three narrow peaks, one of which is a dominant mode. Increasing the noise to 15%, Figures 14 and 15 suggest the presence of two modes, visualizing the structure about them, the MAP estimates and the mean values, compared to the true inclusion and the prior information. One of the modes for the material properties seems reminiscent of the prior values while the other one relates to the true object that generated the data. Additional modes for 5% may be related to the layered structure and the difficulty of resolving the depth. These figures use uniform fixed meshes to evaluate the observation operator. Repeating the
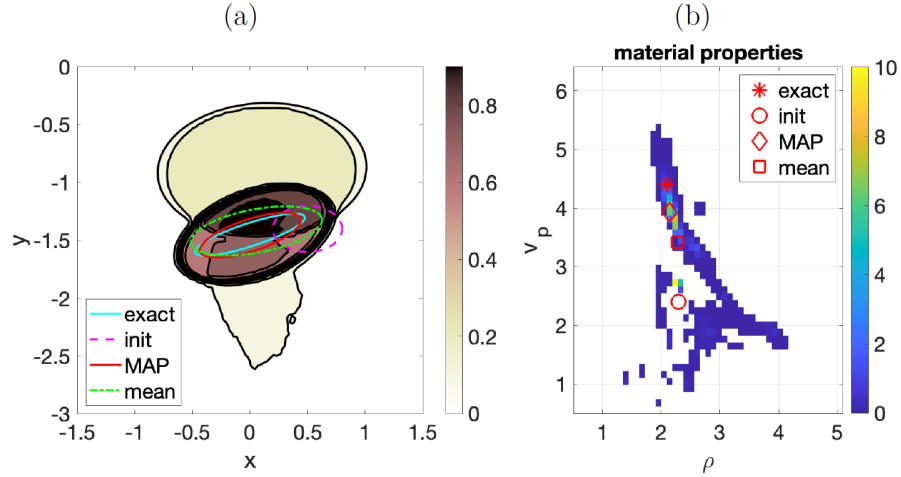
Figure 14: (a) Contour plot of the probability of belonging to the inclusion and (b) projection of the histogram for its material properties (pdf normalization) calculated by MCMC sampling and corresponding to Figure 8(b) with 15% noise.
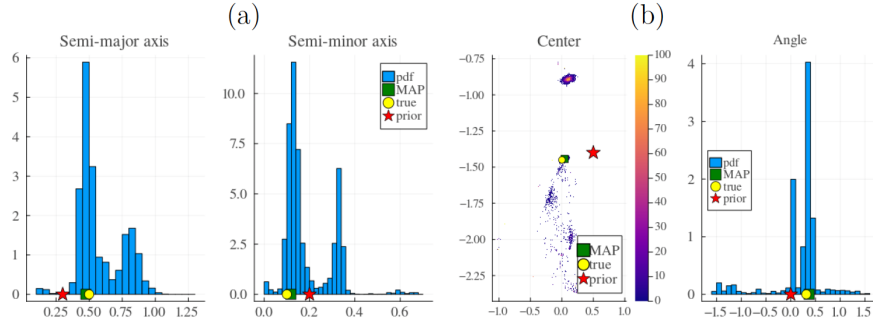

Figure 15: Histograms for axis size (a), centers and angles (b) associated to Figure 14 built from 412.800 samples.

tests keeping the same data with stratified fixed meshes the main features remain similar. We may encounter small additional modes that vary with the mesh, specially for small noise levels in the data. However, the main modes remain similar.

We have repeated these simulations in larger computational domains, increasing the number of receivers and sources, and also in homogeneous media. Working with only one frequency, multiple solutions, ranked by their probability, persist. Adding data obtained with additional frequencies, the main mode agrees for the different frequencies while the secondary modes vary. Resorting to costs /likelihoods combining several frequencies, secondary modes are diluted.

6 Conclusions

Devising computational tools to investigate subsurface structures from surface measurements is a challenging problem, which we have addressed here using complementary strategies to infer details on the observed inclusions from synthetic data. Inclusions are defined by their material parameters and a few additional parameters describing their location, size and orientation. We have applied our algorithms for increasing noise levels in a simplified geometry of current interest involving localized salt inclusions. Salt areas typically hide reservoirs of relevant raw materials.

In a Bayesian context we seek high probability configurations (MAP estimates) by optimizing a cost regularized with prior information and constrained with time dependent wave equations governing wave propagation. First, we propose an automatic adaptive iterative scheme that employs a Levenberg-Marquardt-Fletcher type algorithm with observation operators defined by finite element solvers constructed on meshes that adapt automatically to the proposed objects at each iteration. Variations are estimated using automatic differentiation. In synthetic tests employing a single frequency, this scheme evolves to the global minimum, which represents the MAP estimate of the sought inclusions, except in exceptional situations where additional minima with large attraction basins are encountered. We obtain basic uncertainty estimates in the parameter ranges by means of Laplace approximations. Second, we propose an alternative scheme that approximates observation operators resorting rougher solvers defined on either uniform or stratified meshes. These meshes are kept fixed during the process. We seek descent directions estimating the variations of the solution as the inclusion changes by finite differences with small fixed steps. Depending on the selected step, the algorithm may evolve to the global minimum or secondary local minima, if present.

On one side, adaptive optimization employs more accurate solvers. On the other, changing the mesh at each optimization step we may avoid getting trapped at spurious minima that might appear due to the usage of fixed meshes. In practice, in the tests presented here, the configurations at which the cost attains a global minimum remain similar, no matter whether we use uniform meshes (blind to the layered structure) or stratified meshes (adapted to the layers but not to the inclusion), for fine enough meshes.

Markov Chain Monte Carlo methods have the potential of exploring the whole set of minima of the cost and the multimodal structure of the posterior probability, at the expense of solving a few million boundary value wave problems. Adapting the mesh to each proposed inclusion is not affordable. We are forced to approximate the observation operator keeping a fixed mesh for different inclusions. We find MAP estimates similar to the ones provided by the adaptive optimization scheme in the tests we have performed, except in singular cases in which the prior information allows for secondary minima with a larger attraction basin. This may be the case for elongated horizontal configurations, in which the lower half is screened by the upper half and the dataset we consider may not cover a wide enough range. MCMC studies provide a deeper understanding of uncertainty, since we identify additional high probability configurations. In the tests we have performed, we have usually encountered one mode related to the true inclusion, and often a second mode that seems to keep a memory of

the material parameters of the prior. A third intermediate mode appears occasionally, using either uniform or stratified meshes. Small fluctuations may vary with the mesh, specially when the noise level in the data is small. However, the dominant modes remain similar for the two types of meshes, uniform and stratified, provided they are fine enough, though the latter is expected to reproduce better transmission of waves at interfaces. This is a useful remark since, in practice, we may not know the underlying layered structure and be forced to use blind uniform meshes. This is often the case in high-dimensional studies. This situation remains even if we enlarge the computational region and increase the number of emitters/receivers or we suppress the layers and consider a uniform background.

Notice that our tests use synthetic data generated numerically. Therefore we know beforehand the true inclusions that produce the data. In the tests we have performed the MAP estimate is related to the true object. However, in the absence of a global view of the probability modes that may appear, there is the risk of trusting secondary modes as inaccurate reconstructions. Global uncertainty studies are thus important to clarify these facts and may be useful to guide the design of imaging set-ups for which multimodality is suppressed and uncertainty in the predictions of inclusion properties diminishes. In our set-up, varying the frequency of the emitted signals, the secondary modes vary while the main mode remains. Thus, considering costs/likelihoods that incorporate data recorded with different frequencies, we may suppress secondary minima/modes. Then the results provided by MCMC studies would be fully similar to those automatically obtained by the optimization algorithms and Laplace approximations.

We have focused here on low dimensional descriptions of the inclusions, in the sense that their geometry is described by a few fixed parameters. More precise descriptions involve coefficients belonging to infinite dimensional spaces, often approximated for computational purposes by their values on meshes. This leads to high dimensional problems that can also be treated by optimization and MCMC techniques. Conclusions extracted from low dimensional studies about set-up design to reduce uncertainty and meshes can be useful when dealing with high dimensional formulations.

Appendix A: Nondimensionalization and parameters

To write the forward problem in dimensionless variables we choose two characteristic time T and length L scales. We set $\mathbf{x} = \tilde{\mathbf{x}}L$, $t = \tilde{t}T$, $u = \tilde{u}L$, $R = \tilde{R}L$ and $\Sigma = \tilde{\Sigma}L$. Let us denote $\tilde{\rho} = \frac{\rho}{\rho_0}$, $\tilde{v}_p = \frac{v_p T}{L}$, $\tilde{f}(\tilde{t}) = \frac{T^2}{L} f_0 (1 - 2\pi^2 (f_M T)^2 \tilde{t}^2) e^{-\pi^2 (f_M T)^2 \tilde{t}^2}$ and $\tilde{G}(\tilde{\mathbf{x}}) = \frac{1}{(\pi\kappa)^{n/2}} \sum_{k=1}^{K} \exp(-\frac{|\tilde{\mathbf{x}} - \mathbf{x}_k|^2}{\kappa})$, $n = 2$. We set $T = 1$ s, $L = 1000$ m and $\rho_0 = 1000$ kg/m^3. We choose $f_M = 2$, $f_0 = 100$ so that $f_M T = 2$ and $f_0 \frac{T^2}{L} = 0.1$.

Making the change of variables and dropping the ˜ for ease of notation, we get

$$
\begin{aligned}
\rho u_{tt} - \mathrm{div}(\rho v_p^2 \nabla u) = \rho f(t) G(\mathbf{x}), & \quad \mathbf{x} \in R,\ t > 0, \\
\nabla u \cdot \mathbf{n} = 0, & \quad \mathbf{x} \in \Sigma,\ t > 0, \\
\frac{\partial u}{\partial \mathbf{n}} = -\frac{1}{v_p} u_t, & \quad \mathbf{x} \in \partial R - \Sigma,\ t > 0, \\
u(\mathbf{x}, 0) = 0,\ u_t(\mathbf{x}, 0) = 0, & \quad \mathbf{x} \in R,
\end{aligned}
\tag{18}
$$

where R is the computational rectangular region, Σ the upper surface and v_p stands for the local wave velocity. On $\partial R - \Sigma$ we enforce an approximate nonreflecting boundary condition.

Table 3 collects dimensionless parameter values for Figure 1. The dimensionless computational region becomes $R = [-1.5, 1.5] \times [-3, 0]$. We discretize the problem using FEM meshes of minimum step 0.04 with emitters/receivers interspaced with step 0.02. Emitters are $e_k = -1 + 0.04k$, $k = 0, \ldots, 50$, and receivers $r_j = -1.02 + 0.04j$, $j = 0, \ldots, 51$. The value κ is adjusted to the mesh so that it affects a small region about the emitters. Here we have set $\kappa = 0.04$. The time step for the numerical method is $\delta t = 10^{-3}$ and the profiles are recorded at intervals of 10^{-1}. The maximum time is $T = 2.5$.

Layers	1	2	3	4	5	Object
ρ	2	2.5	2.49	2.49	2.6	2.1
v_p	1.5	2.5	2.8	3.3	3.1	4.4

Table 3: Dimensionless parameter values for the true layered geometry.

We generate synthetic data $\mathbf{d}_{\text{true}}$ for the numerical tests solving numerically (18) and evaluating the approximate solution at the detectors in a fixed time grid. Approximation schemes are described in Appendix C. Then, we corrupt the data with noise to obtain $\mathbf{d}$ according to

$$
d_j^m = d_{j,\text{true}}^m + \frac{r}{100} \sigma \beta,\ j = 1, \ldots, J,\ m = 1, \ldots, M,\ \ \sigma = \Big(\sum_{j=1}^{J} \sum_{m=1}^{M} \frac{|d_{j,\text{true}}^m|^2}{JM} \Big)^{\frac{1}{2}}
$$

where β is drawn from $\mathcal{N}(0, 1)$ and $r > 0$ is the noise level. Then $\sigma_{\text{noise}} = \sigma\, r/100$.

7 Appendix B: Well posedness of the truncated forward problem

We establish next existence, uniqueness and regularity results for solutions of (12) when $\gamma > 0$. We assume that $R \subset \mathbb{R}^n$, $n \geq 2$, is a truncated half-space with borders defined by hyperplanes, that is, a rectangle when $n = 2$ or a parallelepiped when $n = 3$.

We denote by $H^m(R)$ and $L^2(R)$ the standard Sobolev spaces and the space of square-integrable functions, respectively. $L^2(\partial R \setminus \overline{\Sigma})$ is the space of traces on the boundary [42, 29]. Similarly, we denote by $C^m([0, T]; H)$, $m \geq 0$, and $L^\infty([0, T]; H)$

the spaces of continuously differentiable functions up to the order m and bounded functions with values in a Hilbert space H, respectively [42]. For any $u(t) \in H^1(R)$ with $u_t(t) \in L^2(R)$, we define the energy as

$$E(u(t),u_t(t)) = \frac{1}{2}\int_R \rho|u_t|^2 d\mathbf{x} + \frac{1}{2}\int_R \chi|\nabla u|^2 d\mathbf{x} + \frac{1}{2}\int_{\partial R \setminus \overline{\Sigma}} \mu\chi\gamma|u|^2 dS_\mathbf{x}. \qquad (19)$$

Problem (12) admits a weak formulation. Formally, multiplying by $w \in H^1(R)$, integrating by parts over $[0,T] \times R$ and assuming that u is smooth enough, we find

$$\frac{d}{dt^2}\int_R \rho(\mathbf{x})u(t,\mathbf{x})w(\mathbf{x})\,d\mathbf{x} + \int_R \chi(\mathbf{x})\nabla u(t,\mathbf{x})\nabla w(\mathbf{x})\,d\mathbf{x} +$$

$$\frac{d}{dt}\int_{\partial R \setminus \overline{\Sigma}} \chi(\mathbf{x})\gamma(\mathbf{x})u(t,\mathbf{x})w(\mathbf{x})\,dS_\mathbf{x} = \int_R \rho(\mathbf{x})h(t,\mathbf{x})w(\mathbf{x})\,d\mathbf{x} \qquad (20)$$

$$u(0) = u_0, \quad u_t(0) = u_1,$$

for all $w \in H^1(R)$, given $f \in L^\infty(0,T;L^2(R))$. We seek a solution u to (20), at least with regularity $C([0,T];H^1(R)) \cap C^1([0,T];L^2(R))$ to recover (12) in the sense of distributions.

Theorem 1. *Let us assume that*

- $\rho, \chi, \alpha \in L^\infty(R)$, $0 < \rho_{\min} \le \rho \le \rho_{\max}$, $0 < \chi_{\min} \le \chi \le \chi_{\max}$, $0 < \gamma_{\min} \le \gamma \le \gamma_{\max}$,

- $u_0 \in H^1(R)$, $u_1 \in L^2(R)$, $h \in C([0,T];L^2(\Omega))$.

Then, there exists a unique solution $u \in C([0,T];H^1(R)) \cap C^1([0,T];L^2(R))$ to problem (20) with $u_t \in L^2(0,T;L^2(\partial R \setminus \overline{\Sigma}))$. This solution satisfies the wave equation in the sense of distributions. Moreover, it satisfies an energy inequality and depends continuously on the data. The following estimates hold

$$\|u_t\|_{L^\infty(0,T;L^2(R))} \le K(T, \rho_{\min}, \rho_{\max}, E(u_0, u_1), \|h\|_{C([0,T];L^2(R))}),$$

$$\|\nabla u\|_{L^\infty(0,T;L^2(R))} \le K(\chi_{\min}, T, \rho_{\min}, \rho_{\max}, E(u_0, u_1), \|h\|_{C([0,T];L^2(R))}),$$

$$\|u_t\|_{L^2(0,T;L^2(\partial R \setminus \overline{\Sigma}))} \le K(\gamma_{\min}, \chi_{\min}, T, \rho_{\min}, \rho_{\max}, E(u_0, u_1), \|h\|_{C([0,T];L^2(R))}), \qquad (21)$$

$$\|u\|_{L^\infty(0,T;L^2(R))} \le K(\mu, T, \rho_{\min}, \rho_{\max}, E(u_0, u_1), \|h\|_{C([0,T];L^2(R))}),$$

for any $\mu > 0$, where $K(\cdot)$ denote different positive constants depending continuously on the specified arguments.

Proof. The proof is based on the use of Galerkin bases and compactness arguments. When $\gamma = 0$, we can consider a Galerkin basis formed by eigenfunctions of an elliptic operator and prove explicit strong convergence results for the eigenfunction expansion of the solution [51]. However, if $\gamma > 0$, this approach fails, thus, we resort to general abstract bases and compactness arguments next.

Step 1: Galerkin approximation. Since $H^1(R)$ is separable we can always find a set $\{\phi_1, \ldots, \phi_k, \ldots\} \subset H^1(R)$ whose elements are linearly independent while their linear combinations with real coefficients are dense in $H^1(R)$ [42]. For each $M \in \mathbb{N}$, we

27

denote by V^M the space generated by $\{\phi_1, \phi_2, \ldots, \phi_M\}$ and consider the approximate problem: Find $u^M(t, \mathbf{x}) = \sum_{m=1}^{M} a_m(t)\phi_m(\mathbf{x})$ such that

$$\frac{d^2}{dt^2} \int_R \rho u^M(t) w \, d\mathbf{x} + \int_R \chi \nabla u^M(t) \nabla w \, d\mathbf{x} + \frac{d}{dt} \int_{\partial R \setminus \overline{\Sigma}} \chi \gamma \, u^M(t) w \, dS_{\mathbf{x}}$$
$$= \int_R \rho h(t) w \, d\mathbf{x}, \qquad (22)$$

$$u^M(0) = u_0^M, \quad u_t^M(0) = u_1^M.$$

for all $w \in V^M$ and $t \in [0, T]$, see [42], where $u_0^M = \sum_{m=1}^{M} u_{0,m}\phi_m$ and $u_1^M = \sum_{m=1}^{M} u_{1,m}\phi_m$ are the projections of u_0 and u_1 in V^M.

Step 2: Change of variables. To achieve the necessary estimates, we change variables and set $u^M = e^{\mu t} v^M$, $\mu > 0$, so that $u_t^M = \mu e^{\mu t} v^M + e^{\mu t} v_t^M$ and $u_{tt}^M = \mu^2 e^{\mu t} v^M + 2\mu e^{\mu t} v_t^M + e^{\mu t} v_{tt}^M$. Problem (22) becomes: Find $v^M = \sum_{m=1}^{M} b_m(t)\phi_m(\mathbf{x})$ such that

$$\frac{d^2}{dt^2} \int_R \rho v^M(t) w \, d\mathbf{x} + \int_R \chi \nabla v^M(t) \nabla w \, d\mathbf{x} + \frac{d}{dt} \int_{\partial R \setminus \overline{\Sigma}} \chi \gamma \, v^M(t) w \, dS_{\mathbf{x}}$$
$$+ \int_R \rho \mu^2 v^M(t) w \, d\mathbf{x} + \frac{d}{dt} \int_R 2\rho \mu v^M(t) w \, d\mathbf{x} + \int_{\partial R \setminus \overline{\Sigma}} \chi \gamma \mu v^M(t) w \, dS_{\mathbf{x}}$$
$$= e^{-\mu t} \int_\Omega \rho h(t) w \, d\mathbf{x}, \qquad (23)$$

$$v^M(0) = u_0^M, \quad v_t^M(0) = u_1^M,$$

for all $w \in V^M$ and $t \in [0, T]$.

Step 3: Existence of an approximant. Problem (23) is equivalent to a linear system of M second order differential equations for the coefficient functions b_m

$$\sum_{m=1}^{M} b_m''(t) \int_R \rho \phi_m \phi_k \, d\mathbf{x} + \sum_{m=1}^{M} b_m'(t) \left[2\mu \int_R \rho \phi_m \phi_k \, d\mathbf{x} + \int_{\partial R \setminus \overline{\Sigma}} \chi \gamma \, \phi_m \phi_k \, dS_{\mathbf{x}} \right]$$
$$+ \sum_{m=1}^{M} b_m(t) \left[\int_R \chi \nabla \phi_m \nabla \phi_k \, d\mathbf{x} + \mu^2 \int_R \rho \phi_m \phi_k \, d\mathbf{x} + \mu \int_{\partial R \setminus \overline{\Sigma}} \chi \gamma \phi_m \phi_k \, dS_{\mathbf{x}} \right]$$
$$= e^{-\mu t} \int_\Omega \rho h(t) \phi_k \, d\mathbf{x}, \qquad (24)$$

$$b_m(0) = u_{0,m}, \quad b_m'(0) = u_{1,m}, \quad m = 1, \ldots, M,$$

for $k = 1, \ldots, M$. In matricial form,

$$\mathbf{M}\mathbf{b}'' + \mathbf{D}\mathbf{b}' + \mathbf{A}\mathbf{b} = \mathbf{h}(t),$$

where $\mathbf{h}(t) \in C([0, T])$. This linear system can be written as a first order linear system for $\mathbf{b}$ and $\mathbf{a} = \mathbf{b}'$, which has a unique classical solution $\mathbf{b} = (b_1, \ldots, b_m) \in C^2([0, T])$ for any M, see [17], Ch. 3.3.

Step 4: Uniform estimates. We multiply (24) by b_k' and add over k to get

$$\frac{1}{2} \frac{d}{dt} \int_R \rho |v_t^M(t)|^2 d\mathbf{x} + \int_{\partial R \setminus \overline{\Sigma}} \chi \gamma |v_t^M(t)|^2 dS_{\mathbf{x}} + 2\mu \int_\Omega \rho |v_t^M(t)|^2 d\mathbf{x} +$$
$$\frac{1}{2} \frac{d}{dt} \left[\int_R \chi |\nabla v^M(t)|^2 d\mathbf{x} + \mu^2 \int_R \rho |v^M(t)|^2 \, d\mathbf{x} + \mu \int_{\partial R \setminus \overline{\Sigma}} \chi \gamma |v^M(t)|^2 \, dS_{\mathbf{x}} \right] \qquad (25)$$
$$= e^{-\mu t} \int_\Omega \rho h(t) v_t^M(t) \, d\mathbf{x}.$$

28

For any $v(t) \in H^1(R)$ with $v_t(t) \in L^2(R)$, we define the energy as

$$E_\mu(u(t), u_t(t)) = \tfrac{1}{2}\int_R \rho|u_t|^2 d\mathbf{x} + \tfrac{1}{2}\int_R \left[\chi|\nabla u|^2 + \mu^2\rho|u|^2\right] d\mathbf{x} + \tfrac{1}{2}\int_{\partial R\setminus\overline{\Sigma}} \mu\chi\gamma|u|^2 dS_\mathbf{x}. \quad (26)$$

Integrating (25) over t it follows that

$$E_\mu(v^M(t), v_t^M(t)) + \int_0^t \int_{\partial R\setminus\overline{\Sigma}} \chi\gamma|v_t^M(s)|^2 d\mathbf{x}ds + 2\mu \int_0^t \int_R \rho|v_t^M(s)|^2 d\mathbf{x}ds$$

$$= E_\mu(u_0^M, u_1^M) + \int_0^t \int_R e^{-\mu s}\rho h(s)v_t^M(s)\, d\mathbf{x}ds. \tag{27}$$

Discarding positive terms and using the properties of ρ, we find

$$\rho_{\min}\|v_t^M(t)\|_{L^2(R)}^2 \leq \; 2E_\mu(u_0^M, u_1^M) + \rho_{\max}\int_0^t \|h(s)\|_{L^2(R)}^2 ds$$

$$+ \rho_{\max}\int_0^t \|v_t^M(s)\|_{L^2(R)}^2 ds, \tag{28}$$

thanks to Young's inequality. Notice that $E_\mu(u_0^M, u_1^M) \to E_\mu(u_0, u_1)$ as $M \to \infty$ due to strong convergence in $H^1(R)$ and $L^2(R)$. Then, Gronwalls' inequality [15] yields a uniform bound on $\|v_t^M\|_{L^\infty(0,T;L^2(R))}$ in terms of T, $\|h\|$, $E(u_0, u_1)$, and ρ. Inserting this uniform estimate in inequality (27) we obtain uniform bounds on $\|v_t^M\|_{L^2(0,T;L^2(\partial R\setminus\overline{\Sigma}))}$, $\|v^M\|_{L^\infty(0,T;L^2(\partial R\setminus\overline{\Sigma}))}$ and $\|v^M\|_{L^\infty(0,T;H^1(R))}$ when $\mu > 0$.

Step 5: Compactness. By classical compactness results [42, 29], we can extract a subsequence $v^{M'}$ converging weakly star in $W^{1,\infty}(0,T;L^2(R)) \cap L^\infty(0,T;H^1(R))$ to a limit

$$v \in W^{1,\infty}(0,T;L^2(R)) \cap L^\infty(0,T;H^1(R))$$

as $M' \to \infty$, with traces $v_t^{M'}\big|_{\partial R\setminus\overline{\Sigma}}$ converging weakly in $L^2(0,T;L^2(\partial R \setminus \overline{\Sigma}))$ to a limit $v_t\big|_{\partial R\setminus\overline{\Sigma}}$ and $v^{M'}\big|_{\partial R\setminus\overline{\Sigma}}$ converging weakly star $L^\infty(0,T;L^2(\partial R \setminus \overline{\Sigma}))$ to a limit $v\big|_{\partial R\setminus\overline{\Sigma}}$. Moreover, $\frac{d^2}{dt^2}v^{M'} \to \frac{d^2}{dt^2}v$ in the sense of distributions.

Step 6: Passage to the limit. To find the equation satisfied by u, we take $w = \phi_k$, multiply (23) by $\psi(t) \in C_c^\infty([0,T))$ and integrate over t to obtain

$$\int_0^T \int_R \rho v^{M'}\psi_{tt}\phi_k\, d\mathbf{x}ds + \int_R \rho u_{1,m}\psi(0)\phi_k\, d\mathbf{x} - \int_R \rho u_{0,m}\psi_t(0)\phi_k\, d\mathbf{x}$$

$$+ \int_0^T \int_R \chi\nabla v^{M'}\nabla\phi_k\psi\, d\mathbf{x}ds + \int_0^T \int_{\partial R\setminus\overline{\Sigma}} \chi\gamma v_t^{M'}\phi_k\psi\, dS_\mathbf{x}ds$$

$$+ \int_0^T \int_R \rho\mu^2 v^{M'}\phi_k\psi\, d\mathbf{x}ds + \int_0^T \int_R 2\rho\mu v_t^{M'}\phi_k\psi\, d\mathbf{x}ds$$

$$+ \int_0^T \int_{\partial R\setminus\overline{\Sigma}} \chi\gamma\mu v^{M'}\phi_k\psi\, dS_\mathbf{x}ds = \int_0^T e^{-\mu s}\int_R h(s)\phi_k\psi\, d\mathbf{x}ds,$$

for $k \leq M'$. Letting $M' \to \infty$ we find

$$\int_0^T \int_R v\psi_{tt}\phi_k\, d\mathbf{x}ds + \int_R \rho u_1\psi(0)\phi_k\, d\mathbf{x} - \int_R \rho u_0\psi_t(0)\phi_k\, d\mathbf{x}$$

$$+ \int_0^T \int_R \chi\nabla v\nabla\phi_k\psi\, d\mathbf{x}ds + \int_0^T \int_{\partial R\setminus\overline{\Sigma}} \chi\gamma v_t\phi_k\psi\, dS_\mathbf{x}ds$$

$$+ \int_0^T \int_R \rho\mu^2 v\phi_k\psi\, d\mathbf{x}ds + \int_0^T \int_R 2\rho\mu v_t\phi_k\psi\, d\mathbf{x}ds \tag{29}$$

$$+ \int_0^T \int_{\partial R\setminus\overline{\Sigma}} \chi\gamma\mu v\phi_k\psi\, dS_\mathbf{x}ds = \int_0^T e^{-\mu s}\int_R h(s)\phi_k\psi\, d\mathbf{x}ds,$$

for all ϕ_k. The identity extends to all $w \in H^1(R)$ by density. Taking $\psi \in C_c(0, T)$ and $\phi \in C_c(R)$ in (29), and integrating by parts, we see that v satisfies the equation $\rho v_{tt} - \operatorname{div}(\chi \nabla v) + 2\rho\mu v_t + \rho\mu^2 v = e^{-\mu t}h$ in the sense of distributions in $[0, T] \times R$, see [42]. Undoing the change of variables, we have constructed a solution u of

$$\rho u_{tt} - \operatorname{div}(\chi \nabla u) = h \quad \text{in } \mathcal{D}'(0, T) \times R \tag{30}$$

in the sense of distributions.

Since $u \in L^2(0, T; H^1(R))$, $u_t \in L^2(0, T; L^2(R))$ and $u_{tt} \in L^2(0, T; (H(R))')$, after eventually modifying a set of zero measure, $u \in C([0, T]; H^1(R))$ and $u_t \in C([0, T]; L^2(R))$, see Theorem 8.2 in [42], Ch. 3. Then, $u(0) \in H^1(R)$ and $u_t(0) \in L^2(R)$. We take $\psi \in C([0, T))$ and $\phi \in C_c(R)$ in (29), integrate by parts, and use (30), to get $u(0) = u_0$ and $u_t(0) = u_1$. Therefore, we have constructed a solution $u \in C([0, T]; H^1(R)) \cap C^1([0, T]; L^2(R))$ to (12) with $u_t\big|_{\partial R \setminus \overline{\Sigma}} \in L^2(0, T; L^2(\partial R \setminus \overline{\Sigma}))$.

Step 7: Energy inequality. Taking limits in (27) and using the properties of weak convergences we find

$$E_\mu(v(t), v_t(t)) + \int_0^t \int_{\partial R \setminus \overline{\Sigma}} \chi\gamma|v_t(s)|^2 d\mathbf{x}ds + 2\mu \int_0^t \int_R \rho|v_t(s)|^2 d\mathbf{x}ds$$

$$\leq E_\mu(u_0, u_1) + \int_0^t \int_R e^{-\mu s} \rho h(s)v_t(s)\, d\mathbf{x}ds. \tag{31}$$

Undoing the initial change of variables, the function u satisfies a similar inequality with $\mu = 0$:

$$\int_R \rho|u_t(t)|^2 d\mathbf{x} + \int_R \chi|\nabla u(t)|^2\, d\mathbf{x} + 2\int_0^t \int_{\partial R \setminus \overline{\Sigma}} \chi\gamma|u_t(s)|^2 d\mathbf{x}ds$$

$$\leq \int_R \rho|u_1|^2 d\mathbf{x} + \int_R \chi|\nabla u_0|^2\, d\mathbf{x} + 2\int_0^t \int_R h(s)gu_t(s)\, d\mathbf{x}ds. \tag{32}$$

Step 8: Dependence on parameters. Inequality (32) implies

$$\rho_{\min}\|u_t(t)\|_{L^2(R)}^2 \leq \quad 2E(u_0, u_1) + \rho_{\max} \int_0^t \|h(s)\|_{L^2(R)}^2 ds$$

$$+ \rho_{\max} \int_0^t \|u_t(s)\|_{L^2(R)}^2 ds. \tag{33}$$

By Gronwall's inequality, $\|u_t\|_{L^\infty(0,T;L^2(R))}$ is bounded in terms of $\rho_{\min}$, $\rho_{\max}$, T, $E(u_0, u_1)$, and $\|f\|_{L^\infty(0,T;L^2(R))}$. Inserting this information in (32) we obtain similar estimates for $\|\nabla u\|_{L^\infty(0,T;L^2(R))}$ and $\|u_t\|_{L^2(0,T;L^2(\partial R \setminus \overline{\Sigma}))}$ with constants depending also on $\chi_{\min}$ and $\gamma_{\min}$. If we wish to estimate $\|u\|_{L^\infty(0,T;L^2(R))}$ we need to take limits in (27) and (28) with $\mu > 0$ to bound $\|v\|_{L^\infty(0,T;L^2(R))}$, $v = e^{-\mu t}u$, and then $\|u\|_{L^(0,T;L^2(R))}$. The bounding constant depends now also on μ.

Step 9: Uniqueness. Let us consider two solutions w_1 and w_2 with the stated regularity. Then, $u = w_1 - w_2$ is a solution of a similar problem with zero source and zero initial conditions. We perform the change of variables $v = e^{-\mu t}u$ and consider the equation (29) for v. Next, we adapt the uniqueness proof of Theorem 8.1 in [42], Ch. 3. We choose $\tau \in (0, T)$ and take a test function $w(t) = -\int_t^\tau v(\sigma)d\sigma$ when $t < \tau$, zero otherwise. With this choice, $w_t = v \in C([0, T], H^1(R))$ and $w \in C([0, T], H^1(R))$.

Inserting the test function w in (29) instead of $\phi\,\psi$ we get

$$\int_0^T \int_R \left[-\rho v_t w_t - 2\rho\mu v w_t + \chi\nabla v\nabla w + \rho\mu^2 vw \right] d\mathbf{x}ds$$

$$+ \int_0^T \int_{\partial R\setminus\overline{\Sigma}} [-\chi\gamma vw_t + \chi\gamma\mu vw] dS_\mathbf{x}ds = 0,$$

As a result,

$$\int_0^\tau \int_R \left[-\rho v_t v - 2\rho\mu|v|^2 + \chi\nabla w_t\nabla w + \rho\mu^2 w_t w \right] d\mathbf{x}ds$$

$$+ \int_0^\tau \int_{\partial R\setminus\overline{\Sigma}} [-\chi\gamma|v|^2 + \chi\gamma\mu w_t w] dS_\mathbf{x}ds = 0.$$

Integrating we find

$$0 = \tfrac{1}{2}\int_R \left[-\rho|v(\tau)|^2 - \chi|\nabla w(0)|^2 - \rho\mu^2|w(0)|^2 - 2\rho\mu|v|^2 \right] d\mathbf{x}ds$$

$$-\tfrac{1}{2}\int_{\partial R\setminus\overline{\Sigma}} \chi\gamma\mu w(0) dS_\mathbf{x}ds - \int_0^\tau \int_R 2\rho\mu|v|^2 d\mathbf{x}ds - \int_0^\tau \int_{\partial R\setminus\overline{\Sigma}} \chi\gamma|v|^2 dS_\mathbf{x}ds.$$

This implies $v = 0$. Therefore, $u = 0$ and $w_1 = w_2$. $\square$

Corollary 2 (Conditions at interfaces). *Under the hypotheses of Theorem 1, if $h \in C^1([0,T]; L^2(R))$, $u_1 \in H^1(R)$ and $u_2 = \mathrm{div}(\chi\nabla u_0)/\rho + h(0,\mathbf{x}) \in L^2(R)$, the solution $u \in C^1([0,T]; H^1(R)) \cap C^2([0,T]; L^1(R))$ and additional estimates*

$$\|u_{tt}\|_{L^\infty(0,T;L^2(R))} \le K(T, \rho_{\min}, \rho_{\max}, E(u_1,u_2)), \|h_t\|_{C([0,T];L^2(R))}),$$

$$\|\nabla u_t\|_{L^\infty(0,T;L^2(R))} \le K(\chi_{\min}, T, \rho_{\min}, \rho_{\max}, E(u_1,u_2), \|h_t\|_{C([0,T];L^2(R))}), \quad (34)$$

$$\|u_{tt}\|_{L^2(0,T;L^2(\partial R\setminus\overline{\Sigma}))} \le K(\gamma_{\min}, \chi_{\min}, T, \rho_{\min}, \rho_{\max}, E(u_1,u_2), \|h_t\|_{C([0,T];L^2(R))}),$$

hold. Normal derivatives of u at the boundary are defined in $H^{-1/2}$ and u is a weak solution to (12).

Moreover, if $R = \cup_{\ell=1}^L R^\ell$, R^ℓ being disjoint regions where ρ and χ are constan, at each interface Γ separating two adjacent regions

$$\begin{aligned} u^+ &= u^-, & &\text{in } L^2(\Gamma), \\ \chi^-\nabla u^- \cdot \mathbf{n} &= \chi^+\nabla u^+ \cdot \mathbf{n}, & &\text{in } H^{-1/2}(\Gamma), \end{aligned} \quad (35)$$

where $^+$ and $^-$ denote limit values from each side following the direction of unit normal vector $\mathbf{n}$.

Proof. Formally, differentiating (12) and (20) with respect to t, we have a similar variational equation for $v = u_t$ with right hand side $h_t \in C([0,T]; L^2(R))$ and $v(0,\mathbf{x}) = u_1 \in H^1(R)$ and $v_t(0,\mathbf{x}) = \mathrm{div}(\chi\nabla u_0)/\rho + h(0,\mathbf{x}) = u_2 \in L^2(R)$. This problem admits a solution $v \in C([0,T]; H^1(R)) \cap C^1([0,T]; L^2(R))$ satisfying the properties stated in Theorem 1, which must be equal to u_t in a distribution sense. The enhanced regularity implies that, for all t, $-\mathrm{div}(\chi\nabla u(t)) = \rho h(t) - \rho u_{tt}(t) \in L^2(R)$ with traces $u(t)|_{\partial R} \in L^2(\partial R)$. Let us recall that $\mathbf{q}(t) \in L^2(R)$ and $\mathrm{div}(\mathbf{q}(t)) \in L^2(R)$ imply $\mathbf{q} \cdot \mathbf{n} \in H^{-1/2}(\partial R)$, see [3]. Thus $\nabla u \cdot \mathbf{n}$ is defined at boundaries in $H^{-1/2}$. Integrating by parts in (29) and using (30) we find

$$\begin{aligned} \nabla v \cdot \mathbf{n} &= -\gamma(v_t + \mu v) \quad \text{on } \partial R \setminus \overline{\Sigma} & &\Longrightarrow \nabla u \cdot \mathbf{n} = -\gamma u_t \quad \text{on } \partial R \setminus \overline{\Sigma}, \\ \nabla v \cdot \mathbf{n} &= 0 \quad \text{on } \Sigma & &\Longrightarrow \nabla u \cdot \mathbf{n} = 0 \quad \text{on } \Sigma. \end{aligned} \quad (36)$$

Now, consider two adjacent domains R^1 and R^2 with common interface Γ. Given $u \in H^1(R^1 \cup R^2)$, and denoting by u^+, u^- the limit values of u taken from R^1 and $R2$, respectively, we must have $u^+ = u^-$ on Γ in the sense of L^2 traces. Moreover, for any $w \in H_0^1(R^1 \cup R^2)$ we have the identities

$$\sum_{\ell=1}^2 \int_{\Omega^\ell} \chi^\ell \nabla u \nabla w \, d\mathbf{x} \quad - \sum_{\ell=1}^2 \int_{\Omega^\ell} \operatorname{div}(\chi^\ell \nabla u) w \, d\mathbf{x}$$
$$+ {}_{H^{-1/2}(\Gamma)} \langle [\chi^- \nabla u^- - \chi^+ \nabla u^+] \cdot \mathbf{n}, w \rangle_{H^{1/2}(\Gamma)},$$
$$\int_{\Omega^1 \cup \Omega^2} \chi \, \nabla u \nabla w \, d\mathbf{x} \quad = - \int_{\Omega^1 \cup \Omega^2} \operatorname{div}(\chi \nabla u) w \, d\mathbf{x}.$$

Therefore, the transmission relations hold at any discontinuity interface Γ. $\square$

Theorem 3 (Regularity). *Under the hypotheses of Theorem 1 and 2, let us further assume that*

- *$u_0 = u_1 = 0$,*

- *$h(t, \ \mathbf{x}) = f(t)g(\mathbf{x}) \in C^2([0,T]; H^1(R))$, where $f \in C^2([0,T])$ and $g(\mathbf{x}) \in H^1(R)$, with $\frac{\partial g}{\partial \mathbf{n}} = 0$ on Σ, support contained in an upper layer R^1 with upper boundary Σ, a nd vanishing at a positive distance of $\partial R^1 \setminus \Sigma$.*

Then, the solution of (12) satisfies $u \in C^2([0,T]; H^1(R)) \cap C^3([0,T]; L^2(R))$ to problem (12) with $u_t, u_{tt}, u_{ttt} \in L^2(0,T; L^2(\partial R \setminus \overline{\Sigma}))$. The following additional stability estimates hold

$$\|u_{ttt}\|_{L^\infty(0,T;L^2(R))} \le K(T, \rho_{\min}, \rho_{\max}, E(u_2, u_3), \|h_{tt}\|_{C([0,T];L^2(R))}),$$
$$\|\nabla u_{tt}\|_{L^\infty(0,T;L^2(R))} \le K(\chi_{\min}, T, \rho_{\min}, \rho_{\max}, E(u_2, u_3), \|h_{tt}\|_{C([0,T];L^2(R))}), \qquad (37)$$
$$\|u_{ttt}\|_{L^2(0,T;L^2(\partial R\setminus\overline{\Sigma}))} \le K(\gamma_{\min}, \chi_{\min}, T, \rho_{\min}, \rho_{\max}, E(u_2, u_3), \|h_{tt}\|_{C([0,T];L^2(R))}),$$

where $u_2 = f(0)g$, $u_3 = f'(0)g$ and $K(\cdot)$ denote different positive constants depending continuously on the specified arguments. If $g \in H^2(R)$ and $f \in C^3([0,T])$, analogous regularity and estimates hold for u_{tttt}.

Moreover, u has H^2 regularity in the upper layer near Σ. In dimension $n = 2$, u is continuous up to Σ and its values at the receptor points located at Σ are defined, at least during a certain time.

Proof. Differentiating (20) twice with respect to t, we find for $v = u_{tt}$ a similar problem, with right hand side $h_{tt} \in C([0,T]; L^2(R))$ and initial data $v(0,\mathbf{x}) = f(0)g(\mathbf{x}) \in H^1(R)$ and $v_t(0,\mathbf{x}) = f'(0)g(\mathbf{x}) \in L^2(R)$. This yields (37).

Moreover, for each fixed $t > 0$, we have

$$\operatorname{div}(\chi(\mathbf{x})\nabla u(t)) = \rho(\mathbf{x})h(t,\mathbf{x}) - \rho(\mathbf{x})u_{tt}(t) \in L^2(R), \quad \mathbf{x} \in R,$$
$$\nabla u(t) \cdot \mathbf{n} = 0, \qquad\qquad\qquad\qquad\qquad\qquad\quad \mathbf{x} \in \Sigma,$$
$$\nabla u(t) \cdot \mathbf{n} = -\gamma(\mathbf{x})u_t \in L^2(\partial R \setminus \overline{\Sigma}), \qquad\qquad \mathbf{x} \in \partial R \setminus \overline{\Sigma}.$$

Let us consider a smooth function $\eta(x_1, x_2)$ that decreases from 1 when $x_2 \in [0, -\delta]$ to 0 at $x_2 = -2\delta$, $\eta > 0$ small enough, with support of η to be contained in the upper

layer R^1 around the receivers. Then, $w = u\eta$ has support contained in the first layer and satisfies

$$\chi\Delta w = \eta[\rho h(t) - \rho u_{tt}(t)] + 2\chi\nabla u\nabla\eta + \chi u\Delta\eta = r, \quad \mathbf{x} \in R,$$

$$\nabla w \cdot \mathbf{n} = 0, \qquad\qquad\qquad\qquad\qquad\qquad\qquad \mathbf{x} \in \Sigma,$$

$$\nabla w \cdot \mathbf{n} = -\eta\gamma u_t + u\nabla\eta \cdot \mathbf{n} \qquad\qquad\qquad\qquad \mathbf{x} \in \partial R \setminus \overline{\Sigma},$$

and also, $w = 0, \mathbf{x} \in \Sigma_b$, where Σ_b is the bottom wall. For any $g \in L^2(\partial R)$, there exists a function $w_g \in H^2(R)$ such that $\nabla w_g \cdot \mathbf{n} = g$. Setting $w = \tilde{w} + w_g$, we find

$$\chi\Delta\tilde{w}(t) = r - \chi\Delta w_g(t) \in L^2(R),$$

$$\nabla\tilde{w}(t) \cdot \mathbf{n} = 0, \quad \text{on } \partial R.$$

By the regularity results in [29], Ch. 3, the solution $\tilde{w} \in H^2(R)$. Therefore, u has H^2 regularity in a neighborhood of the receivers for a certain time. By Sobolev's injections [29], u is continuous up to the border in that region in dimension $n = 2$. In particular, it is defined at receptor points. $\square$

Let us discuss now how to approximate numerically the solution of the forward problem.

8 Appendix C: Numerical approximation of the truncated forward problem

Applications to inverse problems require solving large amounts of wave problems, therefore, its is desirable to keep the computational cost as low as possible. We discuss here the approximations employed together with their stability and convergence properties.

8.1 Space-time discretization

We resort to finite element dicretizations in space and finite differences in time. Given a spatial mesh and an associated triangulation $\mathcal{T}_{\delta x}$, with maximum time step δx, we build a FEM basis $\{\psi_1, \ldots, \psi_M\}$, $M = M(\delta x)$, of P^1 elements at least. Let V^M be the space spanned by them.

The discretized problem becomes: Find $u^M(t, \mathbf{x}) = \sum_{m=1}^{M} a_m(t)\psi_m(\mathbf{x})$ such that

$$\frac{d^2}{dt^2} \int_R \rho u^M(t)w \, d\mathbf{x} + \int_R \chi\nabla u^M(t)\nabla w \, d\mathbf{x} + \frac{d}{dt} \int_{\partial R \setminus \overline{\Sigma}} \chi\gamma \, u^M(t)w \, dS_\mathbf{x}$$
$$= f(t) \int_R \rho g w \, d\mathbf{x}, \qquad (38)$$

$$u^M(0) = 0, \quad u_t^M(0) = 0,$$

for all $w \in V^M$ and $t \in [0, T]$.

Lemma 4 (Existence of an approximant). *For $f \in C^2([0, T])$ there is a unique function $u^M \in C^2([0, T]; V^M)$ satisfying (38). Moreover, if $f \in C^k([0, T])$, then $u^M \in C^{k+2}([0, T]; V^M)$, $k \geq 1$.*

Proof. Taking $w = \psi_j$, $j = 1, \ldots, M$, (38) is equivalent to a system of ordinary differential equations

$$\sum_{m=1}^{M} a_m''(t) \int_R \rho \psi_m \psi_j \, d\mathbf{x} + \sum_{m=1}^{M} a_m(t) \int_R \chi \nabla \psi_m \nabla \psi_j \, d\mathbf{x}$$

$$+ \sum_{m=1}^{M} a_m'(t) \int_{\partial R \setminus \overline{\Sigma}} \chi \gamma \, \psi_m \psi_j \, dS_{\mathbf{x}} = f(t) \int_R \rho g(\mathbf{x}) \psi_j \, d\mathbf{x}, \tag{39}$$

$$a_m(0) = a_m'(0) = 0, \quad m = 1, \ldots, M.$$

In vector form $\mathbf{B}\mathbf{v}'(t) = -\mathbf{C}\mathbf{a}(t) - \mathbf{E}v(t) + \mathbf{f}(t)\mathbf{h}$, $\mathbf{a}'(t) = \mathbf{b}v(t)$, $\mathbf{v}(0) = \mathbf{a}(0) = 0$, $t \in [0, T]$. Notice that $\mathbf{M}$ is symmetric and positive definite. This linear system of differential equations has a unique solution in $[0, T]$, see [17], whose regularity increases with the regularity of $f(t)$. $\square$

One can also work with more refined variational formulations set in the different domains and connected through an additional bilinear form representing the transmission conditions [3, 14].

Let us consider now the time discretization. We discretize the time derivatives in (38) using centered differences for u_{tt}^M

$$u_{tt}^M(\mathbf{x}, t) \sim \frac{u^M(\mathbf{x}, t+\delta t) - 2u^M(\mathbf{x}, t) + u^M(\mathbf{x}, t-\delta t)}{\delta t^2} + O(\delta t^2),$$

and backward or centered differences for u_t^M

$$u_t^M(\mathbf{x}, t) \sim \frac{u^M(\mathbf{x}, t) - u^M(\mathbf{x}, t-\delta t)}{\delta t} + O(\delta t), \tag{40}$$

$$u_t^M(\mathbf{x}, t) \sim \frac{u^M(\mathbf{x}, t+\delta t) - u^M(\mathbf{x}, t-\delta t)}{2\delta t} + O(\delta t^2). \tag{41}$$

The first choice yields the scheme

$$\int_R \rho \, u^M(t + \delta t) w \, d\mathbf{x} = \int_R \rho \left[2u^M(t) - u^M(t - \delta t) \right] w \, d\mathbf{x}$$

$$- \delta t^2 \int_R \chi \, \nabla u^M(t) \, \nabla w \, d\mathbf{x} + \delta t^2 \int_R \rho f(t) w \, d\mathbf{x} \tag{42}$$

$$- \delta t \int_{\partial R - \Sigma} \rho \chi \gamma \left[u^M(t) - u^M(t - \delta t) \right] w \, dS_{\mathbf{x}}.$$

On a temporal grid $t_n = n \, \delta t$, $n = 0, \ldots, N$, $n\delta t = T$ we approximate $u^M(t_n) = \sum_{m=1}^{M} a_m(t_n)\phi_m$ by $\sum_{m=1}^{M} a_m^n \phi_m$. The coefficients $a_m(t_n)$, $m = 1, \ldots M$, are approximated by the solution a_m^n of the recurrence:

$$\sum_{m=1}^{M} B_{j,m} a_m^{n+1} = \sum_{m=1}^{M} B_{j,m}(2a_m^n - a_m^{n-1}) - \delta t^2 \sum_{m=1}^{M} C_{j,m} a_m^n$$

$$- \delta t \sum_{m=1}^{M} E_{j,m}(a_m^n - a_m^{n-1}) + \delta t^2 f(t_n) h_j, \quad j = 1, \ldots, M, \tag{43}$$

for $m \geq 1$, with $\mathbf{B}, \mathbf{C}, \mathbf{E}, \mathbf{h}$ defined by

$$B_{j,m} = \int_R \rho \psi_m \psi_j \, d\mathbf{x}, \qquad C_{j,m} = \int_R \chi \nabla \psi_m \nabla \psi_j \, d\mathbf{x},$$

$$E_{j,m} = \int_{\partial R \setminus \Sigma} \chi \gamma \psi_j \psi_m \, dS_{\mathbf{x}}, \quad h_j = \int_R \rho g(\mathbf{x}) \psi_j \, d\mathbf{x}, \tag{44}$$

for $j, m = 1, \ldots, M$. Initially, $a_m^0 = a_m(t_0) = 0$ and $a_m^1 = a_m(t_0) + \delta t\, a'_m(t_0) = 0$ for $m = 1, \ldots, M$, as dictated by the initial conditions.

Lemma 5 (Existence of an approximant). *Scheme (43) admits a unique solution a_m^n, $n = 0, \ldots, N$, $m = 1, \ldots, M$.*

Proof. Given two time levels a_m^{n-1} and a_m^n, $n = 0, \ldots, N$, the level $n + 1$ follows directly from relation (43). $\square$

The matrices and vectors involved in system (43) are known and fixed once the spatial mesh and the associated finite element basis are constructed, provided ρ, χ, γ remain unchanged. For a given inclusion, we use the same matrices and vectors in all the temporal steps. If we vary the shape and the material parameters of inclusions, we need to recalculate them. Depending on whether we keep the mesh fixed or update it, we need to remesh and calculate a new function basis too.

8.2 Convergence results

Consider a regular family of triangulations $\mathcal{T}_{\delta x}$ of R with maximum element diameter $\delta x \to 0$. Let us define associate P^1 finite element spaces $V^M \subset H^1(R)$ of dimension $M = M(\delta x) \to \infty$. We introduce the elliptic projection operator $\Pi^M : H^1(R) \to V^M$ that associates to each $v \in H^1(R)$ the solution $\Pi^M v \in V^M$ of the elliptic problem

$$
\begin{aligned}
& a_\mu(v, v^M) = a_\mu(\Pi^M v, v^M), \quad \forall v^M \in V^M, \\
& a_\mu(v, w) = \int_R \chi \nabla v \nabla w d\mathbf{x} + \int_R \rho\mu^2\, vw d\mathbf{x} + \int_{\partial R \setminus \overline{\Sigma}} \chi\gamma\mu\, vw dS_\mathbf{x},
\end{aligned}
\tag{45}
$$

associated to (23).

Theorem 6 (Convergence of the FEM discretization). *Consider the solution $u \in C^2([0,T]; H^1(R))$ of (12) constructed under the hypotheses of Theorems 1-3 and $u^M \in C^2([0,T]; V^M) \subset H^1(R)$ the solutions generated by the FEM scheme (38). Assume that the family of regular triangulations considered satisfies the approximation property*

$$
\lim_{M \to \infty} \inf_{v^M \in V^M} \|v - v^M\|_{H^1(R)} = 0.
\tag{46}
$$

Then, the sequence $(u^M(t), u_t^M(t))$ converges to $(u(t), u_t(t))$ in $H^1(R) \times L^2(R)$ for all $t \in [0, T]$.

Proof. We make the change of variables $u = e^{\mu t} v$ and $u^M = e^{\mu t} v^M$ in the corresponding variational equations. Subtracting (45), we find [51]

$$
\begin{aligned}
& \frac{d^2}{dt^2} \int_R \rho(v^M - \Pi^M v)(t) v^M\, d\mathbf{x} + \frac{d}{dt} \int_R 2\rho\mu(v^M - \Pi^M v)(t) v^M\, d\mathbf{x} \\
& + \frac{d}{dt} \int_{\partial R \setminus \overline{\Sigma}} \chi\gamma\, (v^M - \Pi^M v)(t) v^M\, dS_\mathbf{x} + a((v^M - \Pi^M v)(t), v^M) \\
& = \int_R \rho(I - \Pi^M) v_{tt}(t) v^M\, d\mathbf{x} + \int_R 2\rho\mu(I - \Pi^M) v_t(t) v^M\, d\mathbf{x} \\
& + \int_{\partial R \setminus \overline{\Sigma}} \chi\gamma(I - \Pi^M) v_t(t) v^M\, dS_\mathbf{x}
\end{aligned}
$$

since $v \in C^2([0,T]; H^1(R))$, with zero initial data. The solution $v^M - \Pi^M v$ of this problem satisfies an energy inequality analogous to (31). Applying Young's inequality

to the right hand side, and taking into account the zero initial data, we find

$$E_\mu((v^M - \Pi^M v)(t), (v^M - \Pi^M v)_t(t)) \le C(\rho, \mu, \chi) \int_0^t [\|(I - \Pi^M)v_{tt}(t)\|_{L^2(R)}^2$$

$$+ \|(I - \Pi^M)v_t(s)\|_{L^2(R)}^2 + \|(I - \Pi^M)v_t(s)\|_{L^2(\partial R \setminus \overline{\Sigma})}^2] ds = I^M(t)$$

with E_μ defined in (26). Then, $E_\mu((v - \Pi^M v)(t), (v - v^M)_t(t))$ is bounded from above in terms of $E_\mu((v - \Pi^M v)(t), (v - v^M)_t(t))$ and $I^M(t)$. Condition (46) implies that $E_\mu((v - \Pi^M v)(t), (v - v^M)_t(t)) \to 0$ as $M \to \infty$. Undoing the change, the same is true for u, therefore, the FEM approximation converges to the solution. Notice that we work in a polygonal domain whose external boundary is fixed. $\square$

Remark 1. For functions $v \in H^2(\Omega)$, estimates of the form $\|v - v^M\|_{H^1(R)} \le C\delta x \|v\|_{H^2(R)}$ hold for regular triangulations [51] and P^1 elements, which ensures condition (46) and $o(\delta x)$ convergence. Solutions of (12) with piecewise constant coefficients in subdomains R^ℓ, $\ell)a, \ldots, L$ can reach at best $H^2(R^\ell)$ regularity in each subdomain. No global $H^2(R)$ regularity can be achieved. In general, we can expect convergence when triangulations are made following a domain decomposition approach, that is, they are entirely contained in each region R^ℓ, sharing vertices at the interfaces.

Remark 2. An additional issue regarding convergence of FEM approximations stems from the fact that we must approximate numerically the integrals appearing in (38). Convergence of these approximations is easier to control when the triangulations are contained in each subdomain R^ℓ sharing nodes at interfaces, avoiding triangles partially contained in different subdomains and mesh nodes moving from one subdomain to another as the triangulations are refined.

Lemma 7 (Convergence of the time discretization). *Consider the solution $u^M = \sum_{m=1}^M a_m(t)\phi_m \in C^2([0, T])$ of (38) constructed in Lemma 4. The sequence u_m^n, $n = 0, \ldots, N$ generated by scheme (43) converges in the sense that $\max_{n=0,\ldots,N} \|a_m(t_n) - u_m^n\| \to 0$ as $N \to \infty$.*

Proof. The approximation has truncation error $O(\delta t^2 + \delta t)$. Convergence requires that matrices $2I - \delta t^2 B^{-1} C - \delta t B^{-1} E$ and $I - \delta t B^{-1} E$ have spectral radius smaller than 1. These matrices depend on δx, which determines their size M, thus $\delta t / \delta x$ must remain small enough [36, 51].

Corollary 8 (Convergence of the full discretization). *Let $u \in C^2([0, T]; H^1(R))$ be the solution of (12) constructed under the hypotheses of Theorems 1-3 and $u_n^M \in V^M$, $n = 0, \ldots, N$, the sequences generated by the scheme (43). Then the error $\max_{n=0,\ldots,N} \|u^M(t_n) - u_n^M\|_{H^1}(R)$ tends to zero as $N, M \to \infty$ provided*

- *condition (46) holds in the regular triangulation uniformly for v belonging to a bounded $H^1(R)$ set,*

- *the ratio $\frac{\delta t}{\delta x}$ of the time step δt to the spatial diameter δx of the triangulation is small enough.*

Proof. Consequence of Theorem 6 and Lemma 7. $\square$

Remark 3. When $R = \cup_{\ell=1}^{L} R^{\ell}$, a Courant-Friedrichs-Lewy condition of the form $\delta t \leq \text{Min}_{\ell=1,\ldots,L}\{1/v_{p,\ell}\}\delta x/2$ in terms of the known layer waves speeds [37] preserves stability in the simulations performed here. In the simulations shown here, we have used the second order discretization (41) in the boundary terms, increasing the global approximation order, and still preserving stability while slightly modifying the scheme.

References

[1] B.M. Afkham, Y. Dong, P.C. Hansen, Uncertainty quantification of inclusion boundaries in the context of x-ray tomography SIAM-ASA J. Uncertain. Quantif. 11 (2023) 31-61.

[2] C.Y. Ahn, K. Jeon, Y.K. Ma, W.K. Park, A study on the topological derivative-based imaging of thin electromagnetic inhomogeneities in limited-aperture problems, Inverse Probl. 30 (2014), 105004.

[3] A. Bamberger, R. Glowinski, Q.H. Tran, A Domain decomposition method for the acoustic wave equation with discontinuous coefficients and grid change, SIAM Journal on Numerical Analysis 34 (1997) 603-639.

[4] C.M. Bishop, Pattern Recognition and Machine Learning, Springer, Berlin, 2006.

[5] C. Borges, A. Gillman, L. Greengard. High resolution inverse scattering in two dimensions using recursive linearization, SIAM J. Imaging Sciences, 10 (2017), 641-664.

[6] T. Bui-Thanh, O. Ghattas, An analysis of infinite dimensional Bayesian inverse shape acoustic scattering and its numerical approximation, SIAM/ASA Journal on Uncertainty Quantification 2 (2014) 203-222.

[7] T. Bui-Thanh, O. Ghattas, J. Martin, G. Stadler, A computational framework for infinite-dimensional Bayesian inverse problems. Part I: The linearized case, with application to global seismic inversion. SIAM Journal on Scientific Computing 35 (2013) A2494-A2523.

[8] F. Cakoni, D. Colton, P. Monk, The Linear Sampling Method in Inverse Electromagnetic Scattering, SIAM, 2011.

[9] A. Carpio, T.G. Dimiduk, F. Le Louër, M.L. Rapún, When topological derivatives met regularized Gauss-Newton iterations in holographic 3D imaging, J. Comp. Phys. 388 (2019) 224-251.

[10] A. Carpio, S. Iakunin, G. Stadler, Bayesian approach to inverse scattering with topological priors, Inverse Problems 36 (2020) 105001.

[11] A. Carpio, E. Cebrián, A. Gutiérrez, Object based full waveform inversion for shear elastography, Inverse Problems 39 (2023) 075007.

[12] F. Caubet, M. Godoy, C. Conca, On the detection of several obstacles in 2D Stokes flow: topological sensitivity and combination with shape derivatives, Inverse Probl. Imaging 10 (2016) 327-367.

[13] D. Colton, R. Kress, Inverse Acoustic and Electromagnetic Scattering, Springer, Berlin, 1998.

[14] J. Chabassier, S. Imperiale, Construction and convergence analysis of conservative second order local time discretisation for linear wave equations, ESAIM: M2AN 55 (2021)1507-1543.

[15] T. Cazenave, A. Haraux, An introduction to semilinear evolution equations, Oxford Lecture Series in Mathematics and Its Applications 13, Clarendon Press, Oxford, 1999.

[16] E.T. Chung, T.F. Chan, X.C. Tai Electrical impedance tomography using level set representation and total variational regularization, Journal of Computational Physics 205 (2005) 357-372.

[17] E.A. Coddington, N. Levinson, Theory of ordinary differential equations, McGraw-Hill, New York, 1955.

[18] O. Dorn, D. Lesselier, Level set methods for inverse scattering, Inverse Probl. 22 (2006) R67-R131.

[19] H. Dronkert, G. Remmelts, Influence of salt structures on reservoir rocks in Block L2, Dutch continental shelf. In: H.E. Rondeel, D.A.J, Batjes, W.H. Nieuwenhuijs,(eds): Geology of gas and oil under the Netherlands, Kluwer (Dordrecht): 159-166, 1996.

[20] M.M. Dunlop, Analysis and Computation for Bayesian Inverse Problems, PhD Thesis, Warwick, 2016.

[21] M.M. Dunlop, Y. Yang, Stability of Gibbs posteriors from the Wasserstein loss for Bayesian full waveform inversion, SIAM/ASA Journal on Uncertainty Quantification 9 (2021),1499-1526.

[22] B. Engquist, A. Majda, Radiation boundary conditions for acoustic and elastic wave calculations, Commun. Pur. Appl. Math. 32 (1979) 312-358.

[23] E. Esser, L. Guasch, T. van Leeuwen, A.Y. Aravkin , F.J. Herrmann, Totalvariation regularization strategies in full-waveform inversion SIAM Journal on Imaging Sciences 11 (2018) 376-406.

[24] G.R. Feijoo, A new method in inverse scattering based on the topological derivative, Inverse Probl. 20 (2004) 1819-1840.

[25] A. Fichtner, H.P. Bunge, H. Igel, The adjoint method in seismology - II. Applications: traveltimes and sensitivity functionals, Phys. Earth Planet. Inter. 157 (2006) 105-23.

[26] R. Fletcher, Modified Marquardt subroutine for non-linear least squares, Tech. Rep. 197213, 1971.

[27] W.R. Gilks, S. Richardson, D. Spiegelhalter, Markov chain Monte Carlo in practice, CRC Press, Boca Raton, 1995.

[28] D. Foreman-Mackey, D.W. Hogg, D. Lang, J. Goodman, emcee: The MCMC Hammer, PASP 125 (2013) 306-312.

[29] P. Grisvard, Elliptic Problems in Nonsmooth Domains, Classics Appl. Math. 69, SIAM Philadelphia, 2011.

[30] Z. Guo, M.V. De Hoop, Shape optimization in full waveform inversion with sparse blocky model representations, Proc. Proj. Rev. 1 (2012) 189-208.

[31] M.E. Hassell, T. Qiu, T. Sánchez-Vizuet, F.J. Sayas, A new and improved analysis of the time domain boundary integral operators for the acoustic wave equation, J. Integral Eqs. Appl. 29 (2017), 107-136.

[32] H. Harbrech, T. Hohage, Fast methods for three-dimensional inverse obstacle scattering problems J. Integr. Equ. Appl. 19 (2007) 237-260.

[33] M. Hintermuller, A. Laurain, Electrical impedance tomography: from topology to shape, Control and Cibernetics 37 (2008) 913-933.

[34] T. Hohage, Iterative methods in inverse obstacle scattering: regularization theory of linear and nonlinear exponentially ill-posed problems, PhD thesis, University of Linz, 1999.

[35] T. Hohage, C. Schormann, A Newton-type method for a transmission problem in inverse scattering, Inverse Problems 14 (1998) 1207-1227.

[36] E. Isaacson, H.B. Keller, Analysis of Numerical Methods, Dover Books on Mathematics, 1994.

[37] F. John, Partial Differential Equations, Applied Mathematical Sciences Series 1, Springer-Verlag New York Inc, 1978.

[38] J. Kaipio, E. Somersalo, Statistical and computational inverse problems, Applied Mathematical Sciences 160, Springer, 2006.

[39] A. Kirsch, The MUSIC-algorithm and the factorization method in inverse scattering theory for inhomogeneous media, Inverse problems 18 (2002) 1025–1040.

[40] L.D. Landau, L.M. Lifshitz, Theory of elasticity, Butterworth-Heinemann, Oxford, 3rd Edition, 1986.

[41] A. Litman, L. Crocco, Testing inversion algorithms against experimental data: 3D targets, Inverse Problems 25 (2009) 020201.

[42] J.L. Lions, E. Magenes, Problémes aux limites non homogénes, Dunod, Paris, 1968.

[43] D.J.C. MacKay, Information Theory, Inference and Learning Algorithms, Cambridge University Press, 2003.

[44] J.J. Moré, The Levenberg-Marquardt Algorithm: Implementation and Theory, Lecture Notes in Mathematics 630, G. Watson Ed., Springer, 1978.

[45] J. Nocedal, S. Wright, Numerical optimization, Springer, New York, 1999.

[46] G. Oleaga, Adaptive Julia codes for shape optimization, preprint 2024.

[47] A. Palafox, M.A. Capistrán, J.A. Christen, Point cloud-based scatterer approximation and affine invariant sampling in the inverse scattering problem Math. Methods Appl. Sci 40 (2017) 3393–3403.

[48] P.O. Persson, Mesh Generation for Implicit Geometries, Doctoral Dissertation, MIT, 2005.

[49] P.O. Persson, G. Strang, A Simple Mesh Generator in MATLAB, SIAM Review 46 (2004) 329-345.

[50] N. Petra, J. Martin, G. Stadler, O. Ghattas, A computational framework for infinite-dimensional Bayesian inverse problems: Part II. Stochastic Newton MCMC with application to ice sheet flow inverse problems SIAM J. Sci. Comput. 36 (2014) A1525-55.

[51] P.A. Raviart, J.M. Thomas, Introduction a l'analyse numérique des équations aux dérivées partielles, Masson, Paris, 1983.

[52] J. Revels, M. Lubin, T. Papamarkou, Forward-Mode Automatic Differentiation in Julia. arXiv:1607.07892 [Cs.MS], 2016.

[53] S. Stein, M.Wysession, An Introduction to Seismology, Earthquakes, and Earth Structure, John Wiley & Sons, 2019.

[54] A. M. Stuart, Inverse problems: A Bayesian perspective, Acta Numerica 19 (2010), 451-559.

[55] A. Tarantola, Inverse Problem theory and methods for model parameter estimation, SIAM, Philadelphia, PA, 2005.

[56] J. Tromp, Seismic wavefield imaging of Earth's interior across scales, Nature Reviews Earth & Environment 1 (2020) 40-53.

[57] C. Tsogka, G.P. Papanicolaou, Time reversal through a solid-liquid interface and superresolution, Inverse Problems 18 (2002)1639-57.

[58] J. Virieux, A. Asnaashari, R. Brossier, L. Métivier, A. Ribodetti, W. Zhou, An introduction to full waveform inversion, Encyclopedia of Exploration Geophysics, 2017 SEG.

[59] Y. Yang, B. Engquist, J. Sun, B.F. Hamfeldt, Application of optimal transport and the quadratic Wasserstein metric to full-waveform inversion, Geophysics 83 (2018) 1JF-Z3.

[60] H. Zhu, S. Li, S. Fomel, G. Stadler, O. Ghattas, A Bayesian approach to estimate uncertainty for full-waveform inversion using a priori information from depth migration Geophysics 81 (2016) R307-23.